

Are infrared dark clouds really quiescent?

S. Feng^{1,2}, H. Beuther², Q. Zhang³, Th. Henning², H. Linz², S. Ragan⁴, R. Smith⁵

1. Max-Planck-Institut für Extraterrestrische Physik, Gießenbachstraße 1, D-85748, Garching bei München, Germany

2. Max-Planck-Institut für Astronomie, Königstuhl 17, D-69117, Heidelberg, Germany

3. Harvard-Smithsonian Center for Astrophysics, 60 Garden Street, Cambridge MA 02138, USA

4. School of Physics and Astronomy, The University of Leeds, Leeds, LS2 9JT, UK

5. Jodrell Bank Centre for Astrophysics, School of Physics and Astronomy, University of Manchester, Oxford Road, Manchester, M13 9PL, UK

August 2, 2016

ABSTRACT

Context. The dense, cold regions where high-mass stars form are poorly characterized, yet they represent an ideal opportunity to learn more about the initial conditions of high-mass star formation (HMSF) since high-mass starless cores (HMSCs) lack the violent feedback seen at later evolutionary stages.

Aims. We investigate the initial conditions of HMSF by studying the dynamics and chemistry of HMSCs.

Methods. We present continuum maps obtained from the Submillimeter Array (SMA) interferometry at 1.1 mm for four infrared dark clouds (IRDCs, G28.34S, IRDC 18530, IRDC 18306, and IRDC 18308). For these clouds, we also present line surveys at 1 mm/3 mm obtained from IRAM 30 m single-dish observations.

Results. (1) At an angular resolution of $2''$ ($\sim 10^4$ AU at an average distance of 4 kpc), the 1.1 mm SMA observations resolve each source into several fragments. The mass of each fragment is on average $> 10 M_{\odot}$, which exceeds the predicted thermal Jeans mass of the entire clump by a factor of up to 30, indicating that thermal pressure does not dominate the fragmentation process. Our measured velocity dispersions in the lines obtained by 30 m imply that non-thermal motion provides the extra support against gravity in the fragments. (2) Both non-detection of high-J transitions and the hyperfine multiplet fit of N_2H^+ ($J = 1 \rightarrow 0$), C_2H ($N = 1 \rightarrow 0$), HCN ($J = 1 \rightarrow 0$), and $H^{13}CN$ ($J = 1 \rightarrow 0$) indicate that our sources are cold and young. However, the obvious detection of SiO and the asymmetric line profile of HCO^+ ($J = 1 \rightarrow 0$) in G28.34 S indicate a potential protostellar object and probable infall motion. (3) With a large number of N-bearing species, the existence of carbon rings and molecular ions, and the anti-correlated spatial distributions between N_2H^+/NH_2D and CO, our large-scale high-mass clumps exhibit similar chemical features to small-scale low-mass prestellar objects.

Conclusions. This study of a small sample of IRDCs illustrates that thermal Jeans instability alone cannot explain the fragmentation of the clump into cold ($T \sim 15$ K), dense ($> 10^5 \text{ cm}^{-3}$) cores and that these IRDCs are not completely quiescent.

Key words. Stars: formation; Stars: massive; ISM: lines and bands; ISM: molecules; ISM: abundance; Submillimeter: ISM

1. Introduction

The high temperatures (> 50 K) and densities ($> 10^5 \text{ cm}^{-3}$) in high-mass protostellar objects (HMPOs; Beuther et al. 2002) give rise to a rich spectrum of molecular lines and so HMPOs are fruitful objects for study. Their formation mechanism, however, is still under debate. Before the protostellar objects exist, the so-called high-mass starless (prestellar) cores (HMSCs, Beuther et al. 2009), form in the densest clumps within the infrared-dark clouds (IRDCs). Following the literatures, we define the following structure hierarchy: IRDCs are large-scale filamentary structures (several tens of pc; Jackson et al. 2010; Beuther et al. 2011; Wang et al. 2014); clumps are dense gas on the order of ~ 1 pc (Zhang et al. 2009); HMSCs usually have high density ($n \geq 10^3\text{--}10^5 \text{ cm}^{-3}$, Teyssier et al. 2002; Rathborne et al. 2006; Butler & Tan 2009; Vasyunina et al. 2009; Ragan et al. 2009) and small sizes (on a scale of ~ 0.1 pc). On the smallest scale (~ 0.01 pc), HMSCs harbor some internal structures known as condensations. The prestellar phase of high-mass sources is not observationally well constrained owing to its short duration, to the sources large average distance

(several kpc), and to the characteristically low temperatures ($T < 20$ K, Carey et al. 1998; Sridharan et al. 2005; Pillai et al. 2006; Wang et al. 2008; Wienen et al. 2012; Chira et al. 2013), which lead to little excitation. In fact, even the existence of HMSCs has been questioned (e.g., Motte et al. 2007) until large survey samples were able to constrain the collapse timescale (on the order of 5×10^4 yrs, e.g., Russeil et al. 2010; Tackenberg et al. 2012).

The Herschel guaranteed time key programme “The Earliest Phases of Star Formation (EPoS)” surveyed a sample of 45 IRDCs (Ragan et al. 2012b). This survey revealed several instances of $70 \mu\text{m}$ dark regions corresponding to peaks in submillimeter dust emission from the ATLASGAL¹. These sources are ideal locations to seek for HMSCs (e.g., Beuther et al. 2010; Henning et al. 2010; Linz et al. 2010; Beuther et al. 2012; Ragan et al. 2012b) and are prime targets with which to address several outstanding questions about the starless phase: What is the structure of HMSCs? What governs their

¹ “The APEX Telescope Large Area Survey of the Galaxy” (ATLASGAL) is a large area survey of the galaxy at $870 \mu\text{m}$ (Schuller et al. 2009).

fragmentation (e.g., Zhang et al. 2009; Bontemps et al. 2010; Zhang & Wang 2011; Beuther et al. 2013; Zhang et al. 2015)? Is thermal pressure sufficient to support HMSCs against collapse (e.g., Wang et al. 2011, 2014)? What are the chemical properties of HMSCs, and how do they compare to more advanced phases (e.g., Miettinen et al. 2011; Vasyunina et al. 2011)?

To investigate these questions, we select a sample of four “quiescent”² IRDC candidates from the EPoS sample: G28.34 S, IRDC 18530, IRDC 18306, and IRDC 18308. The kinematic distances (D) range from 3.6 to 4.8 kpc. We describe our Submillimeter Array (SMA) and IRAM 30-meter telescope observations in Section 2 and present the maps in Section 3. Our analyses of the kinematics and chemistry are presented in Section 4, and we summarize in Section 5.

2. Observations

2.1. Submillimeter Array

We carried out four-track observations on our sample with the SMA at 260/270 GHz (1.1 mm) using the extended (EXT) and compact (COMP) configurations (summarized in Table 1). From May to July 2013, we observed two sources per track, which share bandpass and flux calibrators. For all the observations, phase and amplitude calibrations were performed via frequent switch (every 20 min) on quasars 1743-038 and 1751+096. The primary beam size is $48''$. The phase center for each target is pinned down to the $870\mu\text{m}$ ATLASGAL continuum peak (Schuller et al. 2009), which is listed in Table 2. The baselines (BL) range from 16 m to 226 m with six or seven antennas (N_{ant}) on different days, making structure with extent $\geq 10''$ being filtered out. Bandpass calibrations were done with BL Lac (EXT), 3C 279 (EXT, COMP), and 3C 84 (COMP). Flux calibrations were estimated using Neptune (EXT) and Uranus (COMP). The zenith opacities, measured with water vapor monitors mounted on the Caltech Submillimeter Observatory (CSO) or the James Clerk Maxwell Telescope (JCMT), were satisfactory during all tracks with $\tau(225\text{ GHz}) \sim 0.01\text{--}0.3$. Further technical descriptions of the SMA and its calibration schemes can be found in Ho et al. (2004).

The double sideband receiver was employed, and we tuned the center of spectral band 22 in the lower sideband as the rest frequency of the H^{13}CO^+ ($3 \rightarrow 2$) line, 260.255 GHz. Separated by 10 GHz, the frequency coverages are 258.100–261.981 GHz (LSB) and 269.998–273.876 GHz (USB). Each sideband has a total bandwidth of 4 GHz and a native frequency resolution of 0.812 MHz (a velocity resolution of 0.936 km s^{-1}). The frequency resolutions in the spectral windows of 260.221–260.299 GHz and 271.679–271.757 GHz are 0.406 MHz (corresponding to a velocity resolution of 0.468 km s^{-1}); frequency resolution in the spectral windows of 260.041–260.221 GHz and 271.757–271.937 GHz is 1.625 MHz (velocity resolution of 1.872 km s^{-1}).

The flagging and calibration was done with the MIR package³. The imaging and data analysis was conducted with MIRIAD package (Sault et al. 1995). The synthesized beams and 1σ rms of the continuum image from dual-sidebands at each configuration are listed in Table 2, along with the results obtained by combining configurations with natural weighting. We also list the 1σ rms of the primary beam averaged spectrum of each source.

2.2. Single-dish observations with the IRAM 30 m telescope

In addition to the high spatial resolution observations performed with the SMA, we conducted an imaging line survey of our sample with the IRAM 30 m telescope at 1 mm/3 mm. Observations were performed in the on-the-fly mode from May 28 to May 30, 2014, mapping a $1.5' \times 1.5'$ area of each source. A broad bandpass (8 GHz bandwidth for each sideband) of EMIR covers the range of 85.819–93.600 GHz (E0) with a velocity resolution of 0.641 km s^{-1} , and 215.059–222.841 GHz (E2) with a velocity resolution of 0.265 km s^{-1} . After achieving the expected sensitivity, we tuned the band center on May 31 and observed an “extra band” of 85.119–92.900 GHz and 217.059–224.841 GHz to search for more lines. The phase center, the weather conditions, focus, and pointing information⁴ are listed in Table 3. Using a forward efficiency (F_{eff} , 94% at 1 mm and 95% at 3 mm) and a main beam efficiency (B_{eff} , 63% at 1 mm and 81% at 3 mm)⁵, we converted the data from antenna temperature (T_A) to main beam brightness temperature ($T_{\text{mb}} = F_{\text{eff}}/B_{\text{eff}} \times T_A$). The beam of the 30 m telescope is $\sim 12''$ at 1 mm and $\sim 30''$ at 3 mm. We used the Gildas⁶ software for data reduction and the first step line identification⁷ (Table A1). The 1σ rms T_{mb} in the line free channels are 6–8 mK at 3 mm and 26–33 mK at 1 mm.

3. Observational results

3.1. Fragmentation on small scale from SMA observations

As shown in Figure 1, our sources locate on the ATLASGAL $870\mu\text{m}$ continuum peaks of the pc-scale filaments (shown as red contours in the left column). All targets are embedded in the *Herschel* $70\mu\text{m}$ dark clouds (Ragan et al. 2012a), and each of them is away from the $70\mu\text{m}$ bright region at a projected distance of $\sim 1\text{--}2\text{ pc}$ ($1'\text{--}2'$). At an angular resolution of $\sim 2''$ (corresponding to 10^4 AU on linear scales), the 1.1 mm SMA observations resolve each $870\mu\text{m}$ continuum peak into several compact substructures (hereafter “fragments”, plotted as black contours in the middle and right columns of Figure 1). Combined with “natural weighting”, observations with the COMP+EXT configuration achieve a relatively high angular resolution, but high sensitivity only to the compact structures. Observations with the COMP configuration, however, achieve a higher signal-to-noise ratio and recover some extended

² IRDCs are classified as “active” if they host protostellar dominated cores and “quiescent” if they host prestellar dominated cores, depending on whether both 4.5 and $24\mu\text{m}$ emission is detected (Chambers et al. 2009; Rathborne et al. 2010).

³ The MIR package was originally developed for the Owens Valley Radio Observatory, and is now adapted for the SMA, <http://cfa-www.harvard.edu/~cqi/mircook.html>.

⁴ The SMA continuum peak of each source has some shift from its observational phase center. Therefore, we set the 30 m mapping center according to the SMA continuum peak and use Gildas software to “reproject” the SMA offset accordingly.

⁵ <http://www.iram.es/IRAMES/mainWiki/Iram30 mEfficiencies>

⁶ <http://www.iram.fr/IRAMFR/GILDAS>

⁷ The “Weeds” is an extension of Gildas for line identification (Maret et al. 2011).

Table 1: SMA observation toward four IRDCs: I. configurations

Configuration	Date (yyyymmdd)	Source	N _{ant}	BL (m)	Calibrator Bandpass Flux	T _{sys} (K)	$\tau_{225\text{GHz}}$
EXT	20130530	IRDC 18306 IRDC 18308	7	44-226	BL Lac 3C 279	Neptune	200-400 0.05-0.2
EXT	20130611	G28.34 S IRDC 18530	6	68-226	BL Lac 3C 279	Neptune Titan	200-600 0.2-0.3
COMP	20130717	IRDC 18306 IRDC 18308	6	16-69	3C 279 3C 84	Uranus	200-500 0.1-0.25
COMP	20130719	G28.34 S IRDC 18530	6	16-69	3C 279 3C 84	Uranus	100-300 0.01-0.2

Table 2: SMA observations toward four IRDCs: II. phase center of each source and the synthetic image quality at different configurations

Source		G28.34 S	IRDC 18530	IRDC 18306	IRDC 18308
R.A.	[J2000]	18 ^h 42 ^m 47 ^s	18 ^h 55 ^m 30 ^s	18 ^h 33 ^m 32 ^s	18 ^h 33 ^m 35 ^s
Dec.	[J2000]	-04°04′07″	02°17′06″	-08°32′27″	-08°35′53″
<i>D</i>	(kpc)	4.8	4.6	3.6	4.4
<i>V_{lsr}</i>	(km s ⁻¹)	78.4	75.9	54.8	73.7
COMP ^a	(Maj × Min, P.A)	3.47″ × 1.79″, 32.8°	3.29″ × 1.77″, 34.8°	3.28″ × 2.17″, -7.7°	3.26″ × 2.14″, 9.6°
	σ_{conti}^d (mJy/beam)	1.00	0.86	1.28	1.40
	σ_{line}^e (mK)	78	83	146	162
EXT ^b	(Maj × Min, P.A)	0.88″ × 0.69″, -82.2°	0.88″ × 0.67″, -78.9°	0.93″ × 0.79″, -85.4°	0.93″ × 0.79″, -88.6°
	σ_{conti}^d (mJy/beam)	1.26	1.29	1.31	1.29
	σ_{line}^e (mK)	161	167	141	160
COMP+EXT ^c	(Maj × Min, P.A)	2.55″ × 1.51″, 33.5°	2.44″ × 1.49″, 35.1°	1.79″ × 1.56″, 5.9°	1.67″ × 1.50″, 9.6°
	σ_{conti}^d (mJy/beam)	0.97	0.77	0.99	0.98
	σ_{line}^e (mK)	54	65	268	324

Note. *a.* Synthetic beam of compact configuration.

b. Synthetic beam of extended configuration.

c. Synthetic beam of compact+extended configuration, combined with the “natural weighting”.

d. 1 σ rms measured from the continuum map of each source.

e. 1 σ rms measured from the primary beam averaged spectrum of each source, which is converted into brightness temperature.

Table 3: IRAM 30 m observations on the four IRDCs

Source	R.A. [J2000]	Dec. [J2000]	abbrev.	Source	R.A. [J2000]	Dec. [J2000]	abbrev.
G28.34 S	18 ^h 42 ^m 46 ^s .597	-04°04′11″.940	G28.34 S	IRDC 18530	18 ^h 55 ^m 30 ^s .128	02°17′09″.300	18530
IRDC 18306	18 ^h 33 ^m 32 ^s .044	-08°32′28″.620	18306	IRDC 18308	18 ^h 33 ^m 35 ^s .090	-08°36′00″.120	18308

Date ^a (yyyymmdd)	Source	Pointing	Focus	T _{sys} ^b 1mm (K) 3mm (K)		$\tau_{225\text{GHz}}^b$
20140528	G28.34 S, 18530	Saturn, K3-50A, Venus, 1749+096	Saturn, Venus	450-550	115-130	0.5-0.6
20140529	18306, 18530	Saturn, K3-50A, 1749+096	Saturn	270-310	90-110	0.2-0.4
20140530	18306, 18308	Saturn, 1749+096	Saturn	275-285	90-100	0.2-0.4
20140531*	G28.34 S, 18306, 18308	W3OH, 1749+096	W3OH	210-280	90-110	0.1-0.3

Note. *a.* “*” denotes the date when observational bands were tuned from 85.8–93.6 GHz to 85.2–92.9 GHz, and from 215.1–222.8 GHz to 217.0–224.8 GHz.

b. T_{sys} and τ are averaged system temperature and precipitable water vapor in each observation.

structures of the envelope, so they are essential for studying the morphology of the fragments, e.g., size, mass.

We find 2–4 fragments per source with continuum emission levels $> 3\sigma$ rms in both the COMP and COMP+EXT maps. These fragments have typical sizes of 0.05–0.2 pc and masses of 4–62 M_⊙. They are mostly separated at a projected distance of 0.07–0.24 pc (see Table 4 and discussion in Section 4.1). In particular, fragments in G28.34 S and IRDC 18308 are well aligned along the large-scale filamentary direction. The spatial resolution of our observations only allow the “core” structure to be resolved, so we cannot tell whether the cores contain further hierarchic fragments into condensations or stay as monolithic objects in this paper.

3.2. Line survey from IRAM 30 m at 1 mm/3 mm

Our target lines in the SMA observations included cold, dense gas tracers such as H¹³CO⁺ (3 → 2, E_u/k_B = 25 K), H¹³CN (3 → 2, E_u/k_B = 25 K), HN¹³C (3 → 2, E_u/k_B = 25 K), and HNC (3 → 2, E_u/k_B = 26 K). However, none of them has $> 4\sigma$ rms emission at 1.1 mm. Possible explanations for this include the following: (1) These species were tracing the more extended structures which our observations are not sensitive to; (2) Their emission was too faint to detect, given the sensitivity of our SMA observations; or (3) these high-J lines were not yet excited in these young, cold HMSCs. Our new IRAM 30 m line survey now recovers the extended structure information with 3–10 times more sensitivity than the SMA observations. We now detect emission from lower-J transitions of the above species at 3 mm.

3.2.1. Line identification

We present the spectra from each 30 m targeted source in Figure 2. To increase the signal-to-noise ratio for the weak emission in the dark clouds, each spectrum is averaged from a square region ($[20'', 20'']$ to $[-20'', -20'']$ offset) centered on the SMA continuum peak (the mapping center of the 30 m observations). Using the Splatalogue database⁸, we identified 32 lines from 15 species (including 20 isotopologues) in the 16 GHz-broad 1 mm/3 mm band (Table A1, the lines detected only in the extra band are in blue). Most of them are “late depleters”, which have low critical densities, low E_u/k_B , and low binding energies, and thus are hard to deplete onto grain surfaces (Bergin 2003). Although IRDC 18306 is the nearest source in our sample, its lines have the lowest brightness temperatures. In contrast, G28.34 S has the largest number of detected lines with the highest brightness temperatures in our sample, indicating that this source may be chemically more evolved than the others in our sample.

3.2.2. Molecular spatial distribution

When a high-mass star-forming region (HMSFR) is in the early chemical stages, different species trace gas with different temperatures and densities. Therefore, the spatial distribution diversity from different species can tell us the chemical status of a particular host source.

From Figure 2, G28.34 S has the largest number of emission lines, so we use this source for line identification and list all the detections (having emission $> 4\sigma$ rms) in Table A1. The line profiles as plotted in Figure A1 show that some lines have blended multiplets. To account for this multiplicity when mapping the distribution of all identified species in each source, we integrate each line according to its detection and multiplet using the rules below.

- If a line that has $\geq 4\sigma$ detection in a particular source contains a multiplet, we fit the strongest multiplet transitions using the hyperfine-structure (HFS) fit; otherwise, we fit it using a Gaussian profile⁹ (as discussed in Section 4.3.1 and listed in Table A2)¹⁰. Subsequently, we map the integrated intensities of these lines over their velocity range (down to where the line goes into the noise, Table A3).
- If a G28.34 S-detection species has $< 4\sigma$ detection in another particular source, we integrate a total of three channels around the systematic V_{lsr} at the rest frequency of its strongest transition (marked with “*” in Table A3) in that source.

Figure 3 presents the spatial distributions of all the detected species in our sample. We note that the intensity of some lines in the $70\mu\text{m}$ bright sources in our field of view ($\sim 1'$ NE to G28.34S, IRDC 18530, and NW to IRDC 18308) are stronger than in our target $70\mu\text{m}$ dark sources, which makes the spatial

origin of these species hard to judge. Therefore, we plot the contour that marks the half maximum integrated intensity of a particular species (the black contours in Figure 3). In general, most species show the strongest emission towards the $870\mu\text{m}$ continuum peak. We note that molecular emission peaks in IRDC 18306 and IRDC 18308 have a systematic offset of $\sim 5''$ – $10''$ north of the continuum peak. This may be caused by the pointing uncertainties between 30 m and APEX. Nevertheless, comparison among the sources reveals some similarities and special features of the species that we outline in greater detail for different types of chemistry. Figure A1 shows the line profiles and Figure 3 the distributions¹¹.

⁸ A compilation of the Jet Propulsion Laboratory (JPL, <http://spec.jpl.nasa.gov>, Pickett et al. 1998), Cologne Database for Molecular Spectroscopy (CDMS, <http://www.astro.uni-koeln.de/cdms/catalog>, Müller et al. 2005), and Lovas/NIST catalogues (Lovas 2004), <http://www.splatalogue.net>.

⁹ The HFS fit and the Gaussian fit are both based on the Gildas software package, <http://www.iram.fr/IRAMFR/GILDAS/doc/html/class.html>.

¹⁰ For HCN in IRDC18306, we image the $F = 1 \rightarrow 1$ line. For the rest, we image the line with the strongest relative intensity (according to CDMS/JPL line intensity at 300 K, $\ell(300\text{ K})$ in Table A1).

¹¹ Spatial distributions (Figure 3) and line profiles (Figure A1) are ordered by different groups and listed from the bottom left to the upper right.

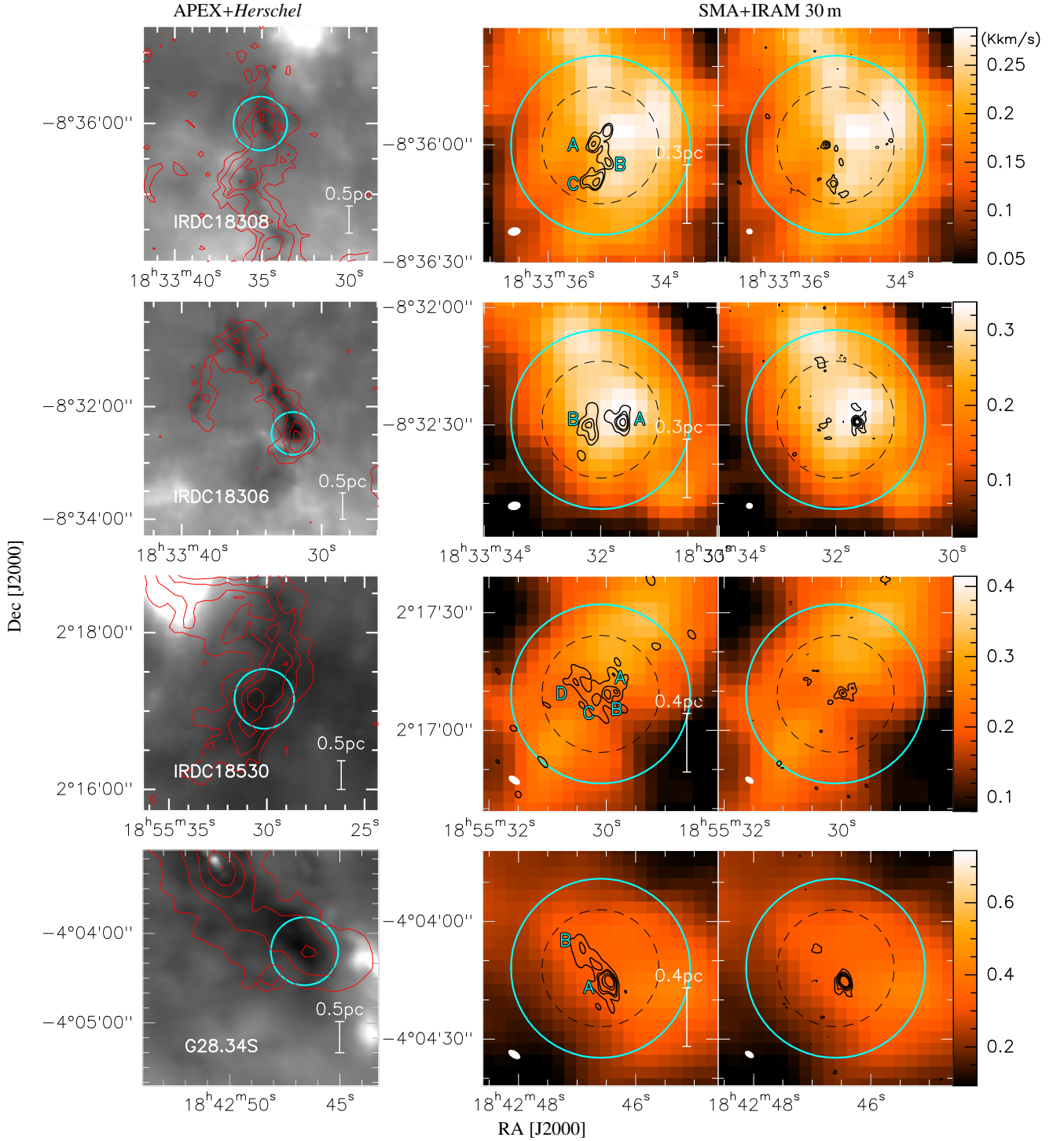


Fig. 1: Compilation of the continuum data from 70 μm to 1.2 mm wavelength for G28.34 S, IRDC 18530, IRDC 18306, and IRDC 18308. Left column: Graymaps of the dust emission observed by *Herschel* at 70 μm (Ragan et al. 2012a). The red contours show continuum emission observed by ATLASGAL at 870 μm (Schuller et al. 2009), starting from 10 σ rms and continuing in 10 σ rms steps. Middle and Right columns: Black contours show continuum observed by SMA COMP configuration (middle) and COMP+EXT combination (right), overlaying the moment 0 colormaps of H¹³CO⁺ (1 \rightarrow 0) (integrated through its velocity dispersion) from IRAM 30 m observations. COMP contours start from 5 σ rms and continue in 5 σ rms steps, while COMP+EXT contours start from 3 σ and continue in 3 σ steps. 1 σ rms of each source configuration is listed in Table 3. Cyan letters mark the fragments having > 3 σ rms continuum emission in both COMP and COMP+EXT maps. In each panel of the middle and right columns, the SMA synthesized beam is in the bottom left. The cyan circles show the primary beam of SMA at 1.1 mm, and the black dashed circles show the beam of 30 m at 3 mm.

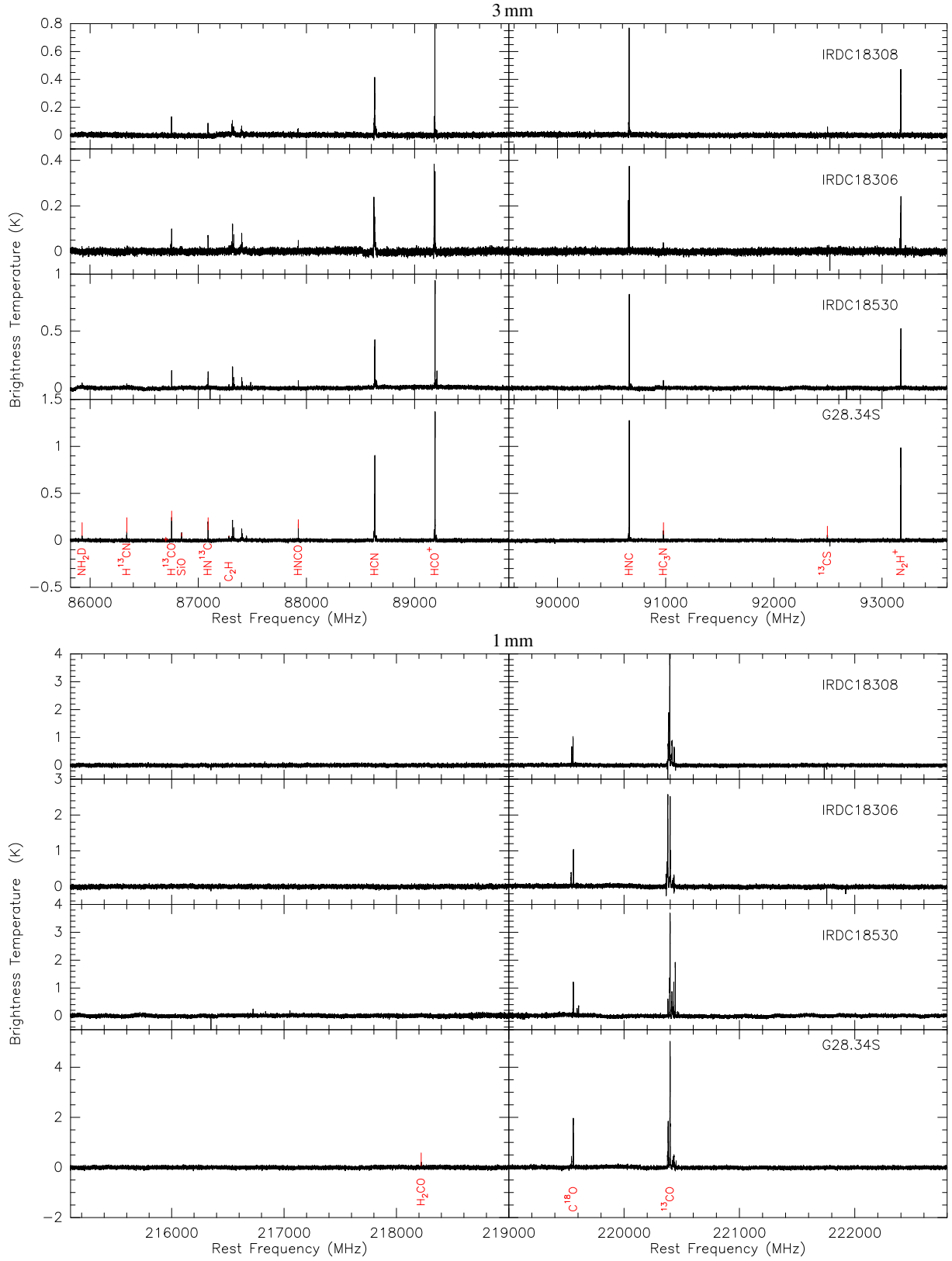


Fig. 2: Averaged spectra from IRAM 30 m line survey at 3 mm/1 mm, which are extracted from a square region ($[20'', 20'']$ to $[-20'', -20'']$ offset) centered on the SMA continuum peak. The spectral resolution is 0.194 MHz (0.265 km s^{-1} at 1 mm and 0.641 km s^{-1} at 3 mm). All detected lines are labeled. The “extra band” is not shown here because of less integration time and thus there is a lower signal-to-noise ratio.

G28.34S

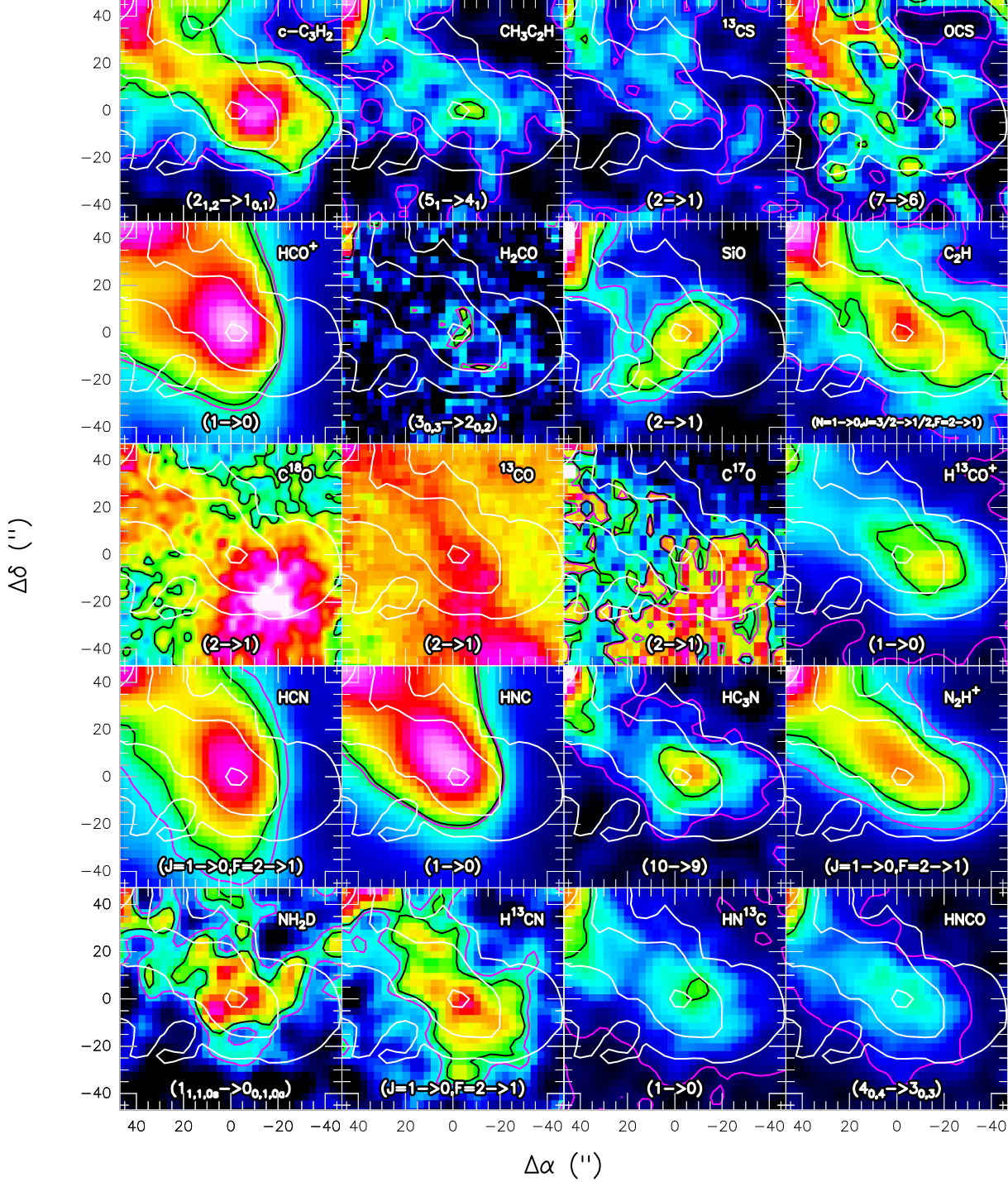


Fig. 3: Molecular line integrated intensity maps overlaid with the $870\mu\text{m}$ continuum contours in G28.34S, IRDC 18530, IRDC 18306, and IRDC 18308. The maps in each source are ordered in different groups according to line rest frequencies and the leading isotopes. Colormaps show the intensity integrations (Kkm s^{-1}) over the velocity dispersion of each line. For the lines with $< 4\sigma$ detections, we only integrate a total of three channels around the system V_{LSR} at their rest frequencies. The purple contour in each panel indicates the area with integrated intensity $> 4\sigma$ rms. The black contour indicates the area within which integrated intensity is over the half maximum in the field of view. The white contours show the continuum emission from $870\mu\text{m}$ ATLASGAL data, starting from 10σ and increasing by 10σ .

IRDC18530

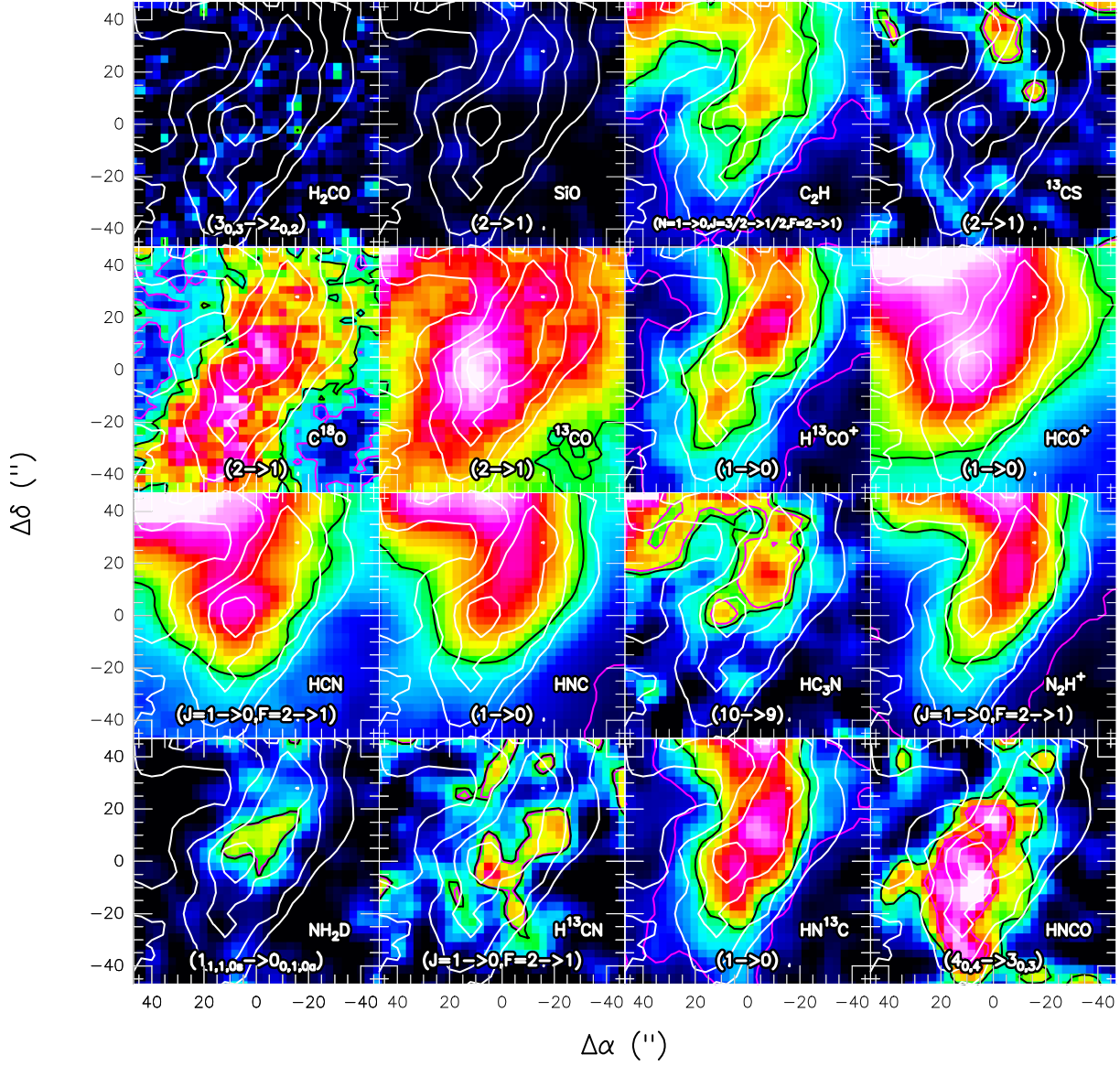


Fig. 3: (continued)

IRDC18306

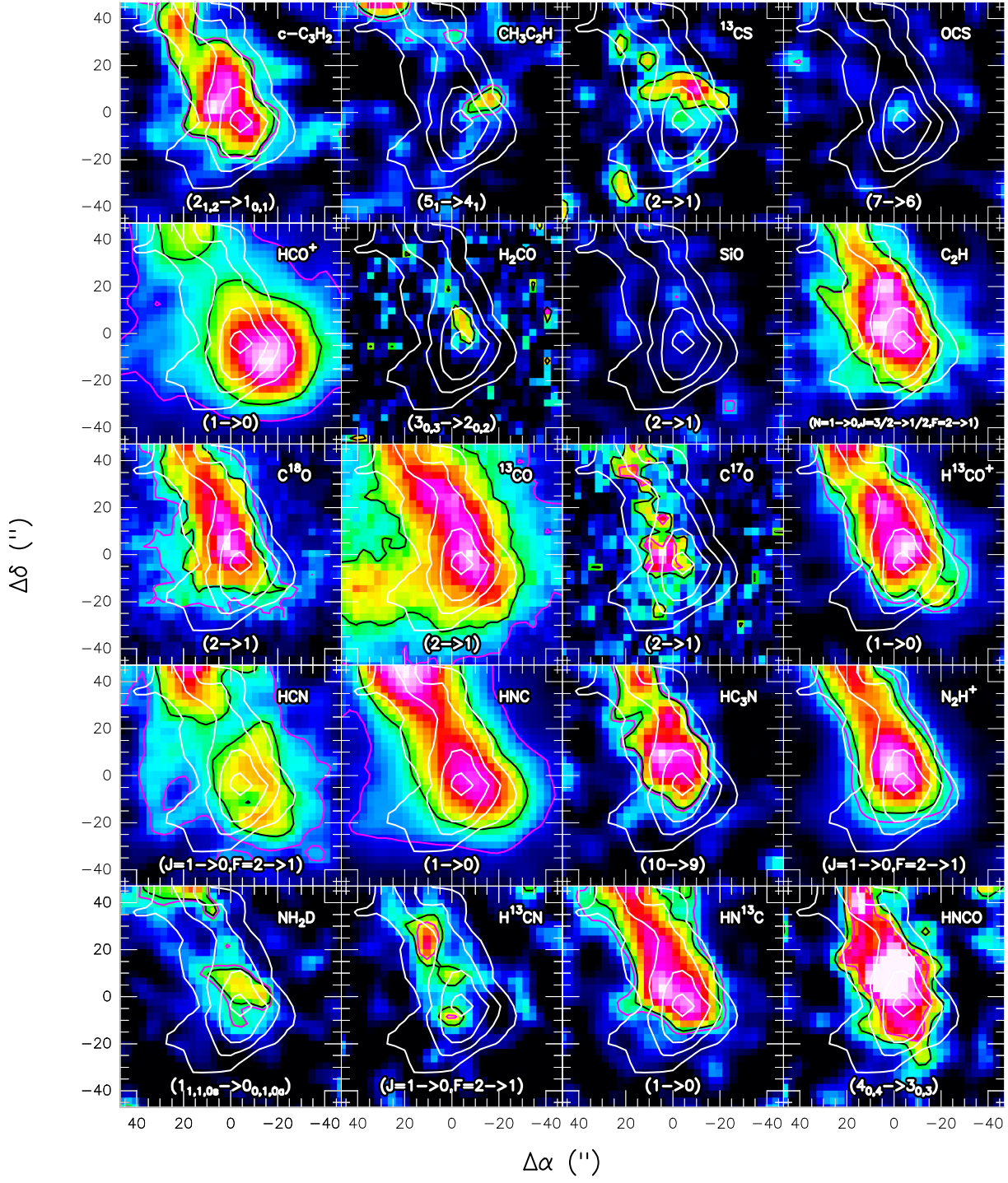


Fig. 3: (continued)

IRDC18308

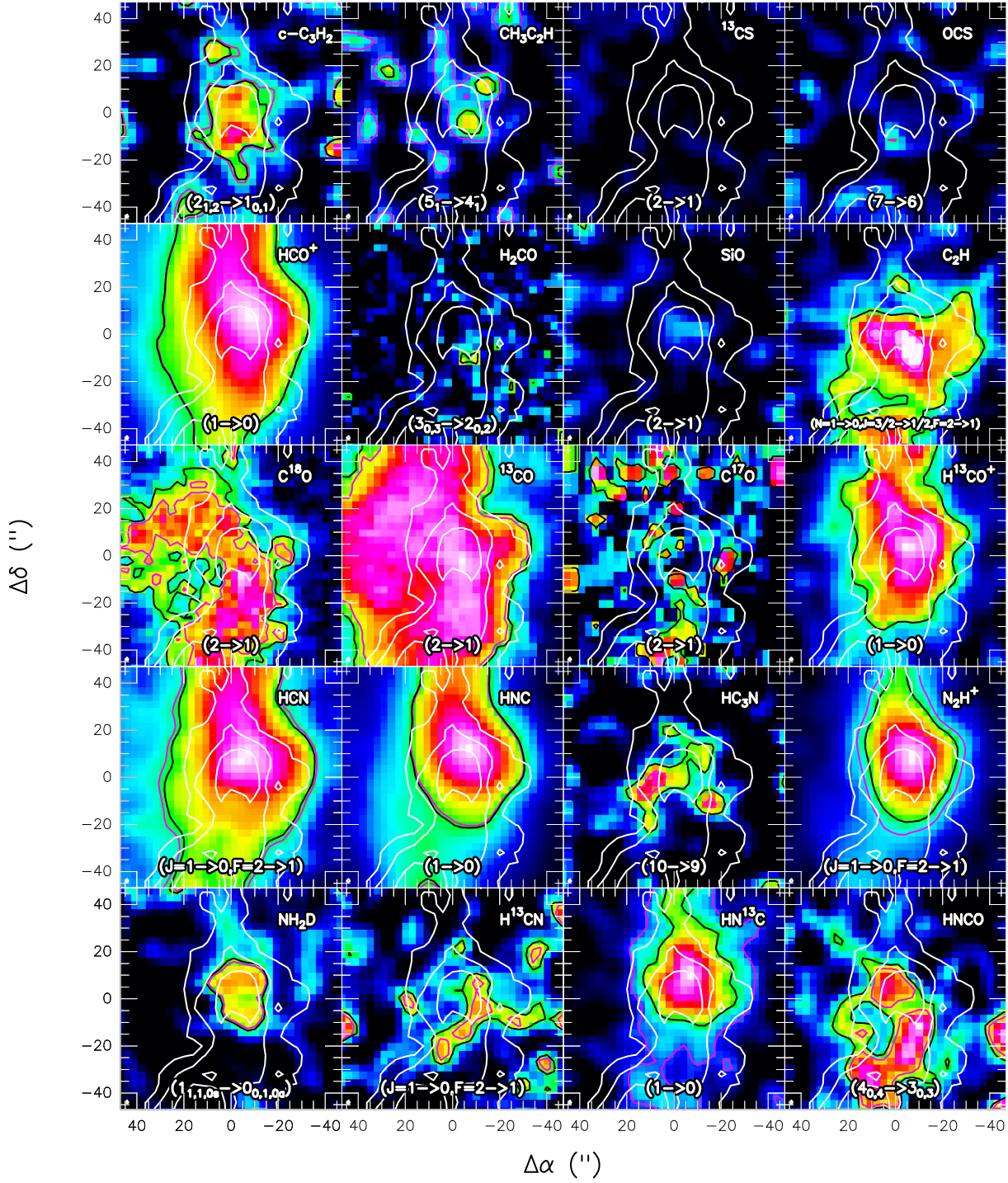


Fig. 3: (continued)

- **Nitrogen (N-) bearing** species have the largest number of lines detected in our 30 m observations. Previous studies especially towards low-mass star-forming regions (e.g., Lee et al. 2001; Pirogov et al. 2003; Fuller et al. 2005; Ragan et al. 2006; Sanhueza et al. 2012; Fontani et al. 2014) show that these species usually trace the cold, dense gas because of their large dipole moments, relatively low optical depths, or simple linear structures (e.g., HC_3N , Bergin et al. 1996). Among them, the abundance of NH_2D can be enhanced by deuteration from NH_3 ($\text{H}_3^+ + \text{HD} \rightarrow \text{H}_2\text{D}^+ + \text{H}_2 + \Delta E$) when CO has frozen out onto the dust grains ($T < 20$ K, Crapsi et al. 2005; Chen et al. 2010; Pillai et al. 2011); HCN (H^{13}CN) is a well-known infall tracer in low-mass prestellar environment (e.g., Sohn et al. 2007); the ratio of HCN/HNC ($\text{H}^{13}\text{CN}/\text{HN}^{13}\text{C}$) is strongly temperature dependent, high in the warmer region like Orion GMC (Goldsmith et al. 1986; Schilke et al. 1992) and approximately around unity (Sarrasin et al. 2010) in the cold environment (see discussion in Section 4.4); multiplets of N_2H^+ are commonly used to reveal the excitation temperature of this species (e.g., Caselli et al. 2002a) in the dark, quiescent regions. All these species have emission peaks or strong emission coincident with the $870\ \mu\text{m}$ continuum peaks, and the offsets between them are less than the pointing uncertainty between 30 m and APEX. In particular, isotopologues of HNC and HCN are co-spatial in sources except for HCN (H^{13}CN) in IRDC 18308. This exception may be explained by the abnormal enhancement or suppression of the individual hyperfine line discussed in Section 4.3.1, indicating non-LTE (local thermal equilibrium) excitations of HCN (Loughnane et al. 2012).

In addition to the simple N-bearing species, HNCO is the simplest organic species containing C, H, O, and N elements. Moreover, it has been suggested as a shock tracer, based on its correlated spatial distribution with SiO (e.g., Zinchenko et al. 2000) and CH_3OH (e.g., Meier & Turner 2005). We found extended emission of HNCO in all our dark, cold clumps. The velocity dispersion of this line is similar to the other lines ($1 - 3\ \text{km s}^{-1}$) on the scale of $0.8\ \text{pc}$, so we are not able to tell whether the shocks are from cloud-cloud collision (e.g., Jiménez-Serra et al. 2009, 2010; Nguyen-Lu'o'ng et al. 2013) or from protostellar objects deeply embedded.

- **Carbon oxidized and hydride species** are important indicators of the chemical status of a particular star-forming region. Because they are one of the most abundant molecules in the gas phase, possessing a low dipole moment and low critical density, CO isotopologues (^{13}CO , C^{18}O , and C^{17}O) can be used to indicate the gas temperature (e.g., Tafalla et al. 1998; Pineda et al. 2008, see also Appendix B). HCO^+ is the typical dense gas tracer produced from CO, and its abundance is enhanced in regions with a high ionization fraction and/or shocked by outflows (e.g., Codella et al. 2001; Hofner et al. 2001; Rawlings et al. 2000, 2004). H_2CO is an important carbon hydride which forms CH_3OH and other more complex organics later in the gas phase (e.g., Horn et al. 2004; Garrod et al. 2008); sublimation of this species needs a warmer environment, so the detection of this species indicates the host cloud may be in a more evolved phase.

These species show the following features in G28.34S: (1) a clear anti-correlated distribution between CO isotopologues

(especially the optically thin $2 \rightarrow 1$ lines of C^{18}O and C^{17}O) and $\text{N}_2\text{H}^+/\text{NH}_2\text{D}/\text{H}^{13}\text{CO}^+$, indicating strong depletion and ionization even on the scale of $0.8\ \text{pc}$ (see discussion in Section 4.5); (2) a blue asymmetric line profile of the optically thick HCO^+ ($1 \rightarrow 0$) comparing to H^{13}CO^+ ($1 \rightarrow 0$), indicating possible large velocity of infall motion (Myers et al. 1996; Mardones et al. 1997, see Figure 4 and Section 4.3 for detailed discussion); and (3) $> 4\sigma$ line emission from H_2CO coincident with the continuum peak, indicating warmer gas there. Despite a tentative anti-correlated distribution between C^{17}O and $\text{N}_2\text{H}^+/\text{H}^{13}\text{CO}^+$ on the scale of $0.5\ \text{pc}$ in IRDC 18308, a $10''$ ($0.2\ \text{pc}$) offset between CO and NH_2D emission peak in IRDC 18308, and a tentative detection of H_2CO (2σ emission) in IRDC 18306, the other sources do not have the same features found in G28.34 S.

We note that the emission peak of HCO^+ ($1 \rightarrow 0$) and H^{13}CO^+ ($1 \rightarrow 0$) are not strictly co-spatial in any source (offsets are $5'' - 10''$), and this may come from the large opacity of HCO^+ . However, H^{13}CO^+ shows a “deficiency” at the continuum peak of IRDC 18530 where ^{13}CO is abundant, which is probably due to the dissociative recombination in this environment (see discussion in Section 4.6).

- **SiO** is a typical shocked gas tracer, and is commonly associated with one or more embedded, energetic young outflows. We detect SiO ($2 \rightarrow 1$) only in G28.34 S, where this line shows strong emission and broad line wings (Figure A1). Coincident with the H_2O maser in G28.34 S (Wang et al. 2006), its emission may be from outflow and thus implies that a protostar is already embedded in this source. However, we cannot rule out the possibility that the SiO emission may also come from the bright infrared source which is $40''$ south of our targeted region, or from G28.34 P1 which is $1'$ to the north and hosts several jet-like outflows (Wang et al. 2011; Zhang et al. 2015). Therefore, the spatial origin of SiO is crucial to diagnose the evolutionary status of G28.34 S, and thus further kinetic study with higher sensitivity data¹² is needed to confirm its spatial origin.
- **Carbon chains/rings** are a mysterious group of species whose gas/grain origin is still not clear. Among the species we detected, C_2H is thought to reside (predicted by chemical models) in the source center in the early stage, before transforming into other species (e.g., CO, OH, H_2O), and it can have high abundance in the outer shells even at later stages (Beuther et al. 2008); the carbon ring $\text{c-C}_3\text{H}_2$, first detected in the cold dark cloud TMC-1 by Matthews & Irvine (1985), is reported to survive even in a hot region where NH_3 is photon-destroyed (Palau et al. 2014); and $\text{CH}_3\text{C}_2\text{H}$ is considered a good probe of temperature for early stages of star-forming regions (Bergin et al. 1994). We detect the above-mentioned carbon chains/ring towards the continuum peak of all our sources, except in IRDC 18530 where only C_2H is observed. However, since these species also show stronger or roughly the same emission towards the nearby $70\ \mu\text{m}$ bright sources (according to the half maximum intensity contour), we cannot tell whether these species are good cold gas tracers or not.

- **Sulfur (S-) bearing species** also have unknown chemistry. Two S-bearing lines, ^{13}CS ($2 \rightarrow 1$) and OCS ($7 \rightarrow 6$) are

¹² The SiO ($6 \rightarrow 5$) line has only 2.5σ detection in our SMA data.

covered in our observations (except for the OCS line in IRDC 18530). Owing to their high dipole moments, CS isotopologues are used as dense gas tracers (e.g., Bronfman et al. 1996) in both low-mass (e.g., Tafalla et al. 2002) and high-mass prestellar cores (e.g., Jones et al. 2008), but they show high depletions in the center of high-mass dense cores (e.g., Beuther & Henning 2009). OCS forms via surface chemistry and is the only S-bearing molecule that has actually been observed on interstellar ices (Palumbo et al. 1997). Both ^{13}CS and OCS are only detected in G28.34 S with $> 4\sigma$ emission, but these emissions have been shown to originate from the NE bright source, according to their half maximum intensity contours. Therefore, we do not claim their spatial origin from the cold gas.

In short, G28.34 S appears chemically more evolved than the other sources in our sample, thanks to the sole detections of H_2CO and OCS, the strong emission of HNCO , the HCO^+ asymmetric line profile implying significant infall, and SiO coinciding with previous H_2O maser detection. All these signatures indicate that G28.34 S is the host of potential protostellar objects.

4. Analysis and discussion

4.1. Fragmentation

Figure 1 presents the continuum maps of *Herschel* 70 μm , APEX 870 μm (ATLASGAL), and SMA 1.1 mm. Because the COMP+EXT configuration of SMA filters out some extended structures, in the following we calculate parameters using data obtained with the COMP configuration only.

We assume that the dust emission is optically thin, and that dust is fully coupled with gas with the same temperature. Therefore, we estimate the mass M_{fr} and column density N_{fr} in the resolved fragments from the SMA continuum maps with (Hildebrand 1983; Schuller et al. 2009):

$$M_{\text{fr}} = \frac{S_{1.1\text{mm}} R D^2}{B_{1.1\text{mm}}(T_{\text{SMA}}) \kappa_{1.1\text{mm}}} \quad (\text{g}) \quad (1)$$

$$N_{\text{fr}} = \frac{I_{1.1\text{mm}} R}{B_{1.1\text{mm}}(T_{\text{SMA}}) \Omega_{\text{SMA}} \kappa_{1.1\text{mm}} \mu m_{\text{H}}} \quad (\text{cm}^{-2}) \quad (2)$$

The averaged column density of the entire clump (in the $40'' \times 40''$ region) N_{c} can be estimated from each ATLASGAL continuum map as well,

$$N_{\text{c}} = \frac{I_{0.87\text{mm}} R}{B_{0.87\text{mm}}(T_{\text{ATLAS}}) \Omega_{\text{ATLAS}} \kappa_{0.87\text{mm}} \mu m_{\text{H}}} \quad (\text{cm}^{-2}), \quad (3)$$

where D is the source kinematic distance (from the sun), $S_{1.1\text{mm}}$ is the total continuum flux density at 1.1 mm (measured from each fragment after a 2-D Gaussian fit¹³, in units of Jy); $I_{1.1\text{mm}}$ is the specific intensity for the continuum peak of each fragment (in Jy beam⁻¹); $I_{0.87\text{mm}}$ is the averaged specific intensity in the $40'' \times 40''$ region (in Jy beam⁻¹); R is the isothermal gas-to-dust mass ratio (taken to be 150, from Draine 2011), $B_{1.1\text{mm}}(T_{\text{SMA}})$ and $B_{0.87\text{mm}}(T_{\text{ATLAS}})$ are the Planck functions for a dust temperature T_{SMA} or T_{ATLAS} ; Ω_{SMA} and Ω_{ATLAS} are the solid angles of the SMA and ATLASGAL beam (in rad²); $\kappa_{1.1\text{mm}} = 1.0 \text{ cm}^2 \text{ g}^{-1}$ and $\kappa_{0.87\text{mm}} = 1.8 \text{ cm}^2 \text{ g}^{-1}$ are the dust absorption coefficients at 1.1 mm and 870 μm (assuming a model of agglomerated grains with thick ice mantles for densities

10^5 – 10^6 cm^{-3} , extrapolated from Ossenkopf & Henning 1994); μ is the mean molecular weight of the ISM, which is assumed to be 2.33; and m_{H} is the mass of a hydrogen atom ($1.67 \times 10^{-24} \text{ g}$).

As described in Table 4, the sizes of fragments (from 2-D Gaussian fitting) are 2–4 times larger than the SMA beam size on small scales. On larger scales, the sizes of filamentary structures (projected area with $> 10\sigma$ emission) seem to be more extended than the primary beam of ATLASGAL ($\theta_{\text{ATLASGAL}} = 18''$). Therefore, we take the filling factors as unity in both spatial scales.

Firstly, we compare the gas concentrations on different spatial scales. Following Kirk et al. (2006), assuming Bonner-Ebert (BE) spheres for both large-scale clumps and small-scale cores, the gas concentration can be estimated in terms of observable parameters as

$$\text{Con}_{\text{ATLAS}} = 1 - \frac{1.44 \Omega_{\text{ATLAS}} \overline{S_{0.87\text{mm}}}}{I_{0.87\text{mm}} A_{0.87\text{mm}}} \quad (4)$$

$$\text{Con}_{\text{SMA}} = 1 - \frac{1.44 \Omega_{\text{SMA}} S_{1.1\text{mm}}}{A_{1.1\text{mm}} I_{1.1\text{mm}}} \quad (5)$$

Here $A_{1.1\text{mm}}$ is the size of each small-scale fragment derived from 2-D Gaussian fits (almost the same size as the area within the 5σ continuum contour). Since ATLASGAL filaments are not suitable to fit with a 2-D Gaussian, we measure the total flux per unit projection size on each ATLASGAL clumps ($\overline{S_{0.87\text{mm}}/A_{0.87\text{mm}}}$) with the following approach. Following Wang et al. (2015), we extract a flux intensity profile from a cut perpendicular to the filament elongated direction, which is centered on the mapping center of the 30 m observations¹⁴. Then we measure the FWHM width of the filament locally around our source. For each filament, we set three rectangles along the filamentary orientation. These rectangles all have the same centers as the previous cut and the same width as the local FWHM width. The length of the rectangles along the filament are one, two, and three times of the FWHM width. Then, we measure the total flux and projection size within each rectangle and derive the mean.

We find that the gas concentration (listed in Tables 4–5) on large scales ($\text{Con}_{\text{ATLAS}} \sim 0.6$) is lower than that in the small-scale fragments ($\text{Con}_{\text{SMA}} \sim 0.8$). Moreover, the large-scale concentration is on the verge of requiring additional non-thermal support mechanism (critical value of BE sphere as 0.72 from Walawender et al. 2005; Kirk et al. 2006).

Secondly, assuming that all small-scale fragments and large-scale cloud clumps are spherically symmetric, we then estimate the gas volume number density of each fragment n_{fr} from θ_{SMA} (in units of rad), and the averaged gas volume number density n_{c} of the entire clump on larger scales from θ_{ATLASGAL} (in units of

¹³ We fit the 2-D Gaussian structure with CASA, <http://casa.nrao.edu>

¹⁴ We assume that the local temperature in the cut is the same at different radii, so the flux intensity profile is the first-order estimate instead of the density profile in Wang et al. (2015).

rad) as¹⁵

$$n_{\text{fr}} = \frac{N_{\text{fr}}}{\theta_{\text{SMA}} D} \quad (\text{cm}^{-3}) \quad (6)$$

$$n_{\text{c}} = \frac{N_{\text{c}}}{\theta_{\text{ATLAS}} D} \quad (\text{cm}^{-3}) \quad (7)$$

We assume that the core-scale structures (size of ~ 0.1 pc) seen in the SMA-COMP configuration result from the fragmentation from the pc-scale clumps. If fragmentation is governed by the thermal Jeans instabilities, the thermal Jeans length $\lambda_{\text{th-J}}$ and mass $M_{\text{th-J}}$ of the entire clump can be estimated from the averaged density and temperature in this clump,

$$\begin{aligned} \lambda_{\text{th-J}} &= c_s \left(\frac{\pi}{G \mu m_{\text{H}} n_{\text{c}}} \right)^{1/2} \\ &= 0.067 \left(\frac{T_{\text{ATLAS}}}{10 \text{ K}} \right)^{1/2} \left(\frac{n_{\text{c}}}{10^5 \text{ cm}^{-3}} \right)^{-1/2} \text{ pc} \end{aligned} \quad (8)$$

$$\begin{aligned} M_{\text{th-J}} &= \frac{c_s^3}{6} \left(\frac{\pi^5}{G^3 \mu m_{\text{H}} n_{\text{c}}} \right)^{1/2} \\ &= 0.912 \left(\frac{T_{\text{ATLAS}}}{10 \text{ K}} \right)^{3/2} \left(\frac{n_{\text{c}}}{10^5 \text{ cm}^{-3}} \right)^{-1/2} M_{\odot}, \end{aligned} \quad (9)$$

where G is the gravitational constant ($6.67 \times 10^{-8} \text{ cm}^3 \text{ g}^{-1} \text{ s}^{-2}$) and $c_s = [k_{\text{B}} T_{\text{ATLAS}} / (\mu m_{\text{H}})]^{1/2}$ is the speed of sound at temperature T_{ATLAS} .

We assume $T_{\text{SMA}} = 15$ K for the following reasons: (1) We did not detect the SMA-targeted lines with low upper energy levels ($E_{\text{u}}/k \sim 25$ K); (2) Low temperatures have been estimated from other observations in G28.34 S, including the SABOCA $350 \mu\text{m}$ survey (13 K as upper limit, $11''$ resolution; Ragan et al. 2013), SPIRE $500 \mu\text{m}$ observations (16 K, $36''$ resolution), and the rotation temperature of NH_3 derived from VLA+Effelsberg (13–15 K, $5''$ resolution, Wang et al. 2008; private communication with K. Wang); (3) It is unclear whether a protostar has already formed in these sources. Dust and gas may either have higher temperature in the envelope region (i.e., structures probed by ATLASGAL, SABOCA, and SPIRE $500 \mu\text{m}$) than at the SMA-probed center because of UV-shielding, or the envelope can be colder than the central core if the protostar has formed (i.e., in G28.34 S). In either case, we give the estimates of the large-scale ATLASGAL clumps at ad hoc temperatures 12 K, 15 K, and 18 K.

As shown in Tables 4–5, the volume number densities in the SMA fragments are at least ten times higher than the averaged volume number densities found in the ATLASGAL clumps. Moreover, the average projected separation between the fragments (0.07–0.24 pc) is comparable to the predicted thermal Jeans length of the entire clump (0.07–0.18 pc) at a temperature of $T_{\text{ATLASGAL}} > 12$ K and $T_{\text{SMA}} \sim 15$ K. However, the fragment masses are significantly higher (more than four times) than the predicted thermal Jeans masses of the entire clumps, even without accounting for interferometric-filtering. In particular, fragment masses are $> 10 M_{\odot}$ in our sample, except for IRDC 18530. A similar discrepancy has also been reported in fragmentation studies in several other IRDCs (e.g., Wang et al. 2014; Beuther et al. 2015).

Different hypotheses have been proposed for the “non-thermal support”, as listed below.

– Turbulent Jeans fragmentation:

Since thermal Jeans fragmentation describes the fragmentation processes when the internal pressure is dominated by the thermal motion, the above-mentioned discrepancy indicates that non-thermal motions, such as turbulence may play an important role in fragmentation (e.g., Wang et al. 2011, 2014).

To investigate whether non-thermal pressure provides extra kinetic energy against the gravitational energy of the fragments, we need to measure the velocity dispersion over the entire clump, which can be derived from the linewidth of the dense gas tracer(s). The linewidths of all the species are on average 2–3 km s^{-1} (see Table A2). H^{13}CO^+ ($1 \rightarrow 0$) has a high critical density ($n_{\text{crit}} > 10^4 \text{ cm}^{-3}$; Bergin & Tafalla 2007; Csengeri et al. 2011; Shirley 2015), low $E_{\text{u}}/k_{\text{B}}$ (4 K), and no hyperfine multiplet. Its velocity dispersion is not affected by Galactic spiral arms (e.g., the line profiles of CO, C^{18}O , and C^{17}O along the line of sight are contributions from various Galactic arms; see Beuther & Sridharan 2007), and it has a symmetric Gaussian profile. Therefore, we use this line to measure the observed velocity dispersion in the line of sight $\sigma_{\text{obs}} = \Delta v / \sqrt{8 \ln 2}$. Here we assume that the averaged gas temperature in the entire clump is $T_{30\text{m}} = T_{\text{ATLAS}}$. Comparing σ_{obs} with the thermally broadened velocity dispersion of H^{13}CO^+ $\sigma_{\text{th}} = \sqrt{8 \ln 2 k_{\text{B}} T_{30\text{m}} / (30 m_{\text{H}})}$, we estimate the non-thermally broadened velocity dispersion $\sigma_{\text{Nth}} = \sqrt{\sigma_{\text{obs}}^2 - \sigma_{\text{th}}^2}$ (see Table 5). Within the gas temperature $T_{30\text{m}}$ range of 12–18 K, we find that σ_{obs} is dominated by non-thermal motions throughout the entire source clump (size of $\sim 10^5$ AU). Therefore, assuming that turbulence dominates the non-thermal motion, we replace c_s with σ_{obs} in Eqs. 8 and 9 and list the turbulent Jeans length $\lambda_{\text{Nth-J}}$ and mass $M_{\text{Nth-J}}$ in Table 5:

$$\begin{aligned} \lambda_{\text{Nth-J}} &= \sigma_{\text{obs}} \left(\frac{\pi}{G \mu m_{\text{H}} n_{\text{c}}} \right)^{1/2} \\ &= 0.35 \left(\frac{\sigma_{\text{obs}}}{\text{km s}^{-1}} \right) \left(\frac{n_{\text{c}}}{10^5 \text{ cm}^{-3}} \right)^{-1/2} \text{ pc} \end{aligned} \quad (10)$$

$$\begin{aligned} M_{\text{Nth-J}} &= \frac{\sigma_{\text{obs}}^3}{6} \left(\frac{\pi^5}{G^3 \mu m_{\text{H}} n_{\text{c}}} \right)^{1/2} \\ &= 136.33 \left(\frac{\sigma_{\text{obs}}}{\text{km s}^{-1}} \right)^3 \left(\frac{n_{\text{c}}}{10^5 \text{ cm}^{-3}} \right)^{-1/2} M_{\odot}. \end{aligned} \quad (11)$$

The above equations do not take magnetic fields into account. In such a regime, the non-thermal motions provide sufficient extra support in the cloud even at low temperatures, and may increase the fragmentation scale. Both $\lambda_{\text{Nth-J}}$ and $M_{\text{Nth-J}}$ are higher than the values observed with SMA, and so this may be a viable method of support. Of course it should be noted that, if the turbulence lead to shocks occurring in the region, the increased density may lead instead to further fragmentation (Dobbs et al. 2005). Note that our data is insufficient to isolate multiple velocity components, given its spectral and spatial resolution. If these are present, the velocity dispersion, and therefore turbulent Jeans length/mass, would be overestimated.

¹⁵ Since both the small-scale fragments and large-scale filaments show asymmetric structures, the simplification 2-D Gaussian fit cannot provide more precise estimation of the volume number density than the method we use here.

Table 4: The parameters measured from SMA observations at 1.1 mm, including the coordinates, specific intensity at continuum peak, total flux density, and projected source size.

Source	R.A. J[2000]	Dec. J[2000]	I_{ν}^a ($\frac{\text{mJy}}{\text{beam}}$)	S_{ν}^a (mJy)	$\theta_{\text{fr}}^{a,b}$ ($'' \times ''$)	Con. ^b	T_{SMA} (K)	N_{fr}^c $10^{23}(\text{cm}^{-2})$	n_{fr}^c $10^5(\text{cm}^{-3})$	λ_{fr}^d (pc)	M_{fr} (M_{\odot})
G28.34 S	18 ^h 42 ^m	-04°04'					15				
	A 46 ^s .426	15'.54	23.5	69.8	5.2'' × 3.6''	0.78		6.38	47.24	0.24	53.45
	B 46 ^s .904	07'.08	8.4	81.4	9.2'' × 6.6''	0.78		2.28	16.88		62.33
IRDC 18530	18 ^h 55 ^m	02°17'					15				
	A 29 ^s .841	09'.87	5.4	8.4	3.6'' × 2.5''	0.77		1.55	12.09	0.07	6.16
	B 29 ^s .983	08'.88	5.3	9.6	3.8'' × 2.7''	0.77		1.52	11.87		7.03
	C 30 ^s .165	07'.81	4.0	8.3	4.5'' × 2.7''	0.78		1.15	8.96		6.08
	D 30 ^s .525	11'.69	3.7	6.5	6.1'' × 1.7''	0.78		1.06	8.29		4.76
IRDC 18306	18 ^h 33 ^m	-08°32'					15				
	A 31 ^s .609	29'.36	13.8	45.3	5.8'' × 4.0''	0.86		5.17	57.39	0.15	21.24
	B 32 ^s .230	29'.58	9.2	71.4	11.2'' × 4.9''	0.86		3.44	38.26		33.49
IRDC 18308	18 ^h 33 ^m	-08°					15				
	A 35 ^s .194	35' 59'.55	8.3	42.6	8.9'' × 4.0''	0.87		3.46	33.24	0.12	29.84
	B 34 ^s .990	36' 04'.53	7.1	78.0	15.5'' × 5.0''	0.87		2.96	28.43		54.64
	C 35 ^s .194	36' 09'.52	11.3	49.8	6.9'' × 4.9''	0.8		4.30	41.25		34.89

Note. *a.* Properties are estimated from the maps with COMP configuration

b. θ_{fr} is from 2-D Gaussian fits

c. H_2 column density and the average volume number density at the continuum peak are estimated at 15 K.

d. λ_{fr} is the mean projected separation of concentrations

Table 5: Parameters from 30 m and APEX observations and estimates based on two hypotheses of fragmentation (thermal Jeans fragmentation and turbulent Jeans fragmentation).

Source	Δv^a (km s^{-1})	σ_{obs}^a (km s^{-1})	$T_{30\text{m}}$ (K)	σ_{th} (km s^{-1})	σ_{Nth} (km s^{-1})	n_c^b (10^5 cm^{-3})	$\lambda_{\text{th-J}}^c$ (pc)	$M_{\text{th-J}}^c$ (M_{\odot})	$\lambda_{\text{Nth-J}}^d$ (pc)	$M_{\text{Nth-J}}^d$ (M_{\odot})	$\lambda_{\text{cl}}^{e,g}$ (pc)	$M_{\text{cl}}^{e,g}$ (M_{\odot})	$(M/l)^{e,g}_{\text{cl}}$ $M_{\odot} \text{ pc}^{-1}$	$(M/l)^{f,g}_{\text{ATLAS}}$ $M_{\odot} \text{ pc}^{-1}$	Con. ^h
G28.34 S	3.07 ± 0.06	1.30 ± 0.03	12	0.14	1.29 ± 0.03	1.07	0.07	1.16	0.45	291	1.57	1240	788	1690 ± 481	0.63 ± 0.04
			15	0.15	1.29 ± 0.03	0.72	0.10	1.97	0.55	354	1.91	1510	788	1146 ± 326	
			18	0.17	1.29 ± 0.03	0.54	0.12	2.99	0.63	409	2.21	1740	788	858 ± 244	
18530	2.01 ± 0.06	0.85 ± 0.03	12	0.14	0.84 ± 0.03	0.79	0.08	1.34	0.34	94.60	–	–	–	–	0.62 ± 0.04
			15	0.15	0.84 ± 0.03	0.54	0.11	2.28	0.41	115	–	–	–	–	
			18	0.17	0.84 ± 0.03	0.40	0.14	3.47	0.48	133	–	–	–	–	
18306	2.05 ± 0.10	0.87 ± 0.04	12	0.14	0.86 ± 0.04	0.85	0.08	1.30	0.34	97.10	–	–	–	–	0.64 ± 0.07
			15	0.15	0.86 ± 0.04	0.57	0.11	2.21	0.41	118	–	–	–	–	
			18	0.17	0.85 ± 0.04	0.43	0.14	3.36	0.47	136	–	–	–	–	
18308	2.09 ± 0.09	0.89 ± 0.04	12	0.14	0.88 ± 0.04	0.52	0.10	1.67	0.44	132	1.54	561	365	391 ± 34	0.60 ± 0.07
			15	0.15	0.87 ± 0.04	0.35	0.14	2.83	0.53	160	1.87	681	365	265 ± 23	
			18	0.17	0.87 ± 0.04	0.26	0.18	4.30	0.62	185	2.16	787	365	198 ± 17	

Note. *a.* Measured from $H^{13}\text{CO}^+$ ($1 \rightarrow 0$) in a $40'' \times 40''$ region (from $[20'', 20'']$ to $[-20'', -20'']$ offset, corresponding to $\sim 1.5 \times 10^5$ AU) obtained from 30 m observations.

b. n_c is measured from ATLASGAL dust emission at $870 \mu\text{m}$.

c. Thermal Jeans length ($\lambda_{\text{th-J}}$) and mass ($M_{\text{th-J}}$) are predicted from ATLASGAL dust emission at $870 \mu\text{m}$.

d. Turbulent Jeans length ($\lambda_{\text{Nth-J}}$) and mass ($M_{\text{Nth-J}}$) are predicted from 30 m observations on $H^{13}\text{CO}^+$ ($1 \rightarrow 0$).

e. The critical mass and length of cylindrical fragmentation are predicted from 30 m observations on the velocity dispersion of $H^{13}\text{CO}^+$ ($1 \rightarrow 0$), Eqs. 12–14.

f. The linear mass densities at different dust temperatures (assuming $T_{\text{ATLAS}} = T_{30\text{m}}$) are predicted from ATLASGAL dust emission at $870 \mu\text{m}$.

g. The values in IRDC 18306 and IRDC 18308 are not given, because the fragments in each source do not align well along the large-scale filamentary direction.

h. Concentration of the gas in the filamentary scale is estimated from ATLASGAL dust emission at $870 \mu\text{m}$ (temperature independent).

The large-scale filamentary gas distribution at $870 \mu\text{m}$ and the small-scale SMA fragments in G28.34 S and IRDC 18308 are well aligned with roughly the same projected separation (Figure 1). Similar feature has been reported in other HMSFRs, e.g., G28.34 S P1 (Zhang et al. 2009; Wang et al. 2011), G11.11-0.12 (Wang et al. 2014), and NGC 7538 S (Feng et al. 2016). Simulations (e.g., Chandrasekhar & Fermi 1953; Nagasawa 1987; Bastien et al. 1991; Inutsuka & Miyama 1992; Fischera & Martin 2012) also predicted that isothermal, “cylindrical” gas collapses into a chain of fragments, with equal spatial separation λ_{cl} along the filament under self gravity, and then the fragments grow due to “varicose” or “sausage” fluid instability (Jackson et al. 2010). Without magnetic fields, the critical linear mass density $(M/l)_{\text{crit}}$ represents the linear mass over which self-gravity overcomes the internal thermal and non-thermal pressure. The critical separation λ_{cl} and critical mass of fragment M_{cl} in the large-scale clump were originally given in Chandrasekhar & Fermi (1953); Nagasawa

(1987). In the case that the thermal motions are not sufficient to be against gravitational energy, we replace the sound speed with the velocity dispersion σ_{obs} , and have (Fiege & Pudritz 2000; Wang et al. 2014):

$$(M/l)_{\text{crit}} = 2\sigma_{\text{obs}}^2/G$$

$$= 465.02 \left(\frac{\sigma_{\text{obs}}}{1 \text{ km s}^{-1}} \right)^2 M_{\odot} \text{ pc}^{-1} \quad (12)$$

$$\lambda_{\text{cl}} = 22\sigma_{\text{obs}}(4\pi G \mu m_{\text{H}} n_c)^{-1/2}$$

$$= 1.25 \left(\frac{\sigma_{\text{obs}}}{1 \text{ km s}^{-1}} \right) \left(\frac{n_c}{10^5 \text{ cm}^{-3}} \right)^{-1/2} \text{ pc} \quad (13)$$

$$M_{\text{cl}} = (M/l)_{\text{crit}} \lambda_{\text{cl}}$$

$$= 580.38 \left(\frac{\sigma_{\text{obs}}}{1 \text{ km s}^{-1}} \right)^3 \left(\frac{n_c}{10^5 \text{ cm}^{-3}} \right)^{-1/2} M_{\odot} \quad (14)$$

In Table 5, we list the critical mass and separation of each source estimated from cylindrical fragmentation. Non-thermal motions, such as turbulence in this special case, can provide support against gravitational collapse of the mass

up to $\sim 800 M_{\odot}$. In particular, the hypothesis of cylindrical fragmentation predicts high linear mass densities for both G28.34 S ($788 M_{\odot} \text{pc}^{-1}$) and IRDC 18308 ($365 M_{\odot} \text{pc}^{-1}$), which are similar to that of IRDC G11.11-0.12 found in Kainulainen et al. (2013) and Wang et al. (2014). These predictions are upper limits, because possible unresolved velocity components may lead to an overestimation of the H^{13}CO^+ velocity dispersion from the 30 m observations (at the angular resolution of $30''$).

To compare the predicted upper limit with the values from observations, we also measure the linear mass of the above ATLASGAL filamentary clumps (M/l)_{ATLAS} from their dust emission maps¹⁶ at the angular resolution of $18''$. We find that if G28.34 S is warmer than 18 K ($855 \pm 244 M_{\odot} \text{pc}^{-1}$) and IRDC 18308 is warmer than 15 K ($265 \pm 23 M_{\odot} \text{pc}^{-1}$, Table 5), the predicted upper limits are higher than the observed linear mass of the ATLASGAL sources. If magnetic field were taken into account, the predicted linear mass would be even higher (e.g., Kirk et al. 2015), i.e., both clumps are likely stable against cylindrical fragmentation.

– Other possibilities:

We do not find obvious velocity gradients in our sources, so the rotation energy is negligible compared to the gravitational energy¹⁷. Nevertheless, other factors in addition to non-thermal motions may also lead to a “mass/separation discrepancy” between the observations and thermal Jeans predications, where the projected separation between the fragments are comparable to the Jeans length, but the observed mass is higher than the Jeans mass. The possible factors are the following:

- (1) Magnetic fields may suppress fragmentation (e.g., Commerçon et al. 2011).
- (2) An inhomogeneous density profile in the core may alter its fragmentation properties. For example, recent numerical simulations by Girichidis et al. (2011) show that less fragmentation occurs in steeper initial density profiles, and the final fragments are more massive than from a flat initial density profile (by a factor of up to 20 in the extreme case).
- (3) The “precise” Jeans length is difficult to quantify. Since the sensitivity of the SMA observations does not detect lower mass fragments, the separation between the fragments is an upper limit of the Jeans length. Conversely, the projection of a 3-D distribution onto the the plane of the sky reduces the observed fragment separation, which makes the measured length a lower limit of the Jeans length. It is difficult to assess quantitatively how these two factors affect the measured separation between dust peaks. These uncertainties make the Jeans length comparison problematic.
- (4) As the density increases, the local Jeans mass decreases, cores can fragment further. Therefore, based on the current data, we cannot rule out the possibility of unresolved

internal sub-fragments (condensations).

In short, the mass of the initial fragments resolved from 1.1 mm SMA observation are already high (on average $> 10 M_{\odot}$). Thermal energy alone cannot compete against the self-gravity of these fragments; however, the combination of thermal and non-thermal motions can provide sufficient energy in opposing the further fragmentation. Moreover, a steep initial density profile of the entire clump and the magnetic field may also increase the upper limit of the final fragment mass. With the current data, it is difficult to measure the precise Jeans length and resolve internal substructures in the fragments. Therefore, we cannot differentiate between the above scenarios.

4.2. Infall motion

We find that the line profiles of HCO^+ ($1 \rightarrow 0$), which is likely optically thick, shows an asymmetric non-Gaussian profile, especially in G28.34 S. In contrast, H^{13}CO^+ ($1 \rightarrow 0$), which is optically thin, shows a fairly symmetric profile (Figure 4). Following Mardones et al. (1997), we measure the normalized velocity difference between the two lines $\delta V_{\text{H}^{13}\text{CO}^+} = (V_{\text{HCO}^+} - V_{\text{H}^{13}\text{CO}^+}) / \Delta v_{\text{H}^{13}\text{CO}^+}$ in each source. Except for IRDC 18308, $\delta V_{\text{H}^{13}\text{CO}^+}$ in other sources are significant¹⁸ (Table 8), indicative of violent dynamics. In particular, line profile of HCO^+ ($1 \rightarrow 0$) in G28.34 S shows double intensity peaks of blue- and redshifted gas, indicating a potential infall motion, with an infall speed $\sim 0.84 \text{ km s}^{-1}$ (derived by using Eq. 9 of Myers et al. 1996). Nevertheless, we note that the peak intensity of the redshifted gas is only 0.1 as strong as that of the blueshifted gas, so we cannot rule out the possibility that double intensity peaks comes from multiple velocity components. If this is the case, the high-velocity (redshifted) gas of H^{13}CO^+ ($1 \rightarrow 0$) may be too weak for the observation sensitivity.

4.3. Molecular column density and abundance estimates

We did not detect emissions of the higher-J molecular transitions in the fragments from the SMA observations. However, the lower-J transitions of the dense gas tracers are detected in the extended structures in the 30 m line survey. This indicates that our sources are in the cold, young phase. To probe the chemical properties in these gas clumps, we quantify their excitation conditions and molecular abundances in this section.

4.3.1. Molecular excitation temperatures and column densities

We calculated the molecular column densities averaged from the central $40'' \times 40''$ region of each source. Since the optical depth may lead to large uncertainties of certain lines, we use different methods to correct their opacities.

- N_2H^+ , C_2H , HCN , and H^{13}CN have multiplets in their $J = 1 \rightarrow 0$ or $N = 1 \rightarrow 0$ (C_2H) transitions. We use the HFS method to fit these transitions (Figure 5) and list their excitation temperatures T_{ex} in Table 6 (see Appendix A for details).

¹⁶ Since a 2-D Gaussian is not suitable for modeling a filamentary structure, we use the same algorithm that measures the total flux per unit projection size to measure the linear masses in rectangles, which are centered on the mapping center of 30 m observations and individually have lengths that are one, two, or three times the local FWHM width, and then derive the mean.

¹⁷ Even if the velocity distribution of our source is biased by our field of view, rotation energy is in general not comparable to the gravitational energy (Goodman et al. 1993; Bihr et al. 2015).

¹⁸ Following the method in Mardones et al. (1997), we set the threshold of “significance” as 5 times the uncertainty of $\delta V_{\text{H}^{13}\text{CO}^+}$.

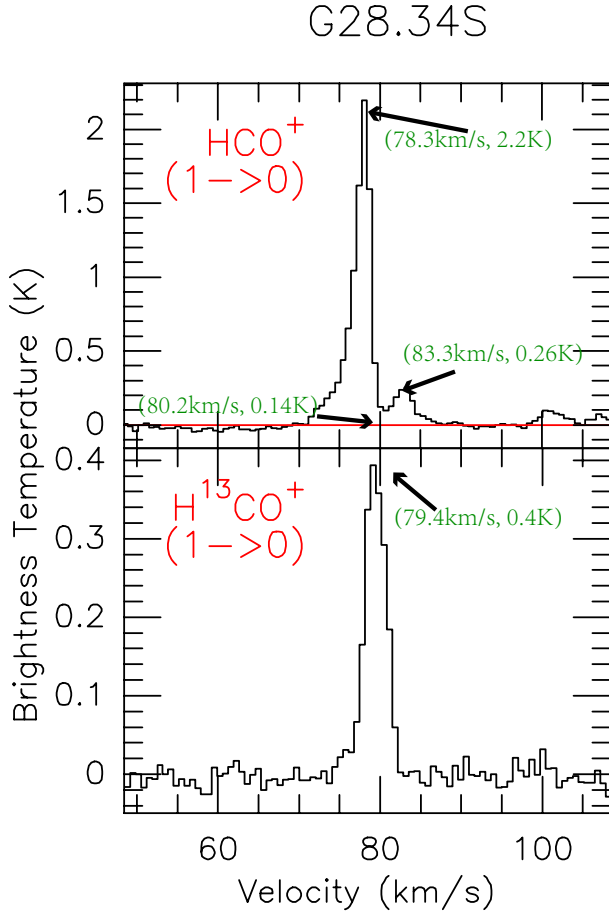


Fig. 4: Asymmetric line profile of $\text{HCO}^+(1 \rightarrow 0)$ compared to $\text{H}^{13}\text{CO}^+(1 \rightarrow 0)$ in G28.34 S, indicating infall motion with a speed of $\sim 0.84 \text{ km s}^{-1}$.

From the fits, we find that the linewidths of the strongest components $\Delta\nu$ of the above species are in the range of $1.7\text{--}3.2 \text{ km s}^{-1}$. This is consistent with the linewidths of the other species (Table A2), indicating that non-thermal motions dominate the velocity dispersion. N_2H^+ ($J = 1 \rightarrow 0$) and C_2H^+ ($N = 1 \rightarrow 0$) are fitted very well, but the fits for HCN ($J = 1 \rightarrow 0$) and H^{13}CN ($J = 1 \rightarrow 0$) show strong deviations. Most of the T_{ex} we derived from the HFS fits are below 10 K (except for HCN in G28.34 S), which could be due to multiple factors:

(1) In the cold gas environment with densities of $10^4\text{--}10^5 \text{ cm}^{-3}$, species with high critical densities are subthermally excited (e.g., at 10 K, the critical density of N_2H^+ ($J = 1 \rightarrow 0$) is $\sim 6 \times 10^4 \text{ cm}^{-3}$, and that of HCN ($J = 1 \rightarrow 0$) is $\sim 5 \times 10^5 \text{ cm}^{-3}$; Shirley 2015), so their T_{ex} is lower than the typical kinetic temperatures of IRDCs (e.g., Sridharan et al. 2005; Vasyunina et al. 2011; Fontani et al. 2012). This feature is common in both high-mass and low-mass dark clouds (e.g., Caselli et al. 2002b; Crapsi et al. 2005; Miettinen et al. 2011; Fontani et al. 2012).

(2) To increase the signal-to-noise ratio for the weak emission, we extract the average spectra from the $40'' \times 40''$ region, but the gas is not homogeneous as assumed. For one thing, H^{13}CN is deficient at the continuum peak of IRDC 18530 and IRDC 18308 (Figure 3). In addition,

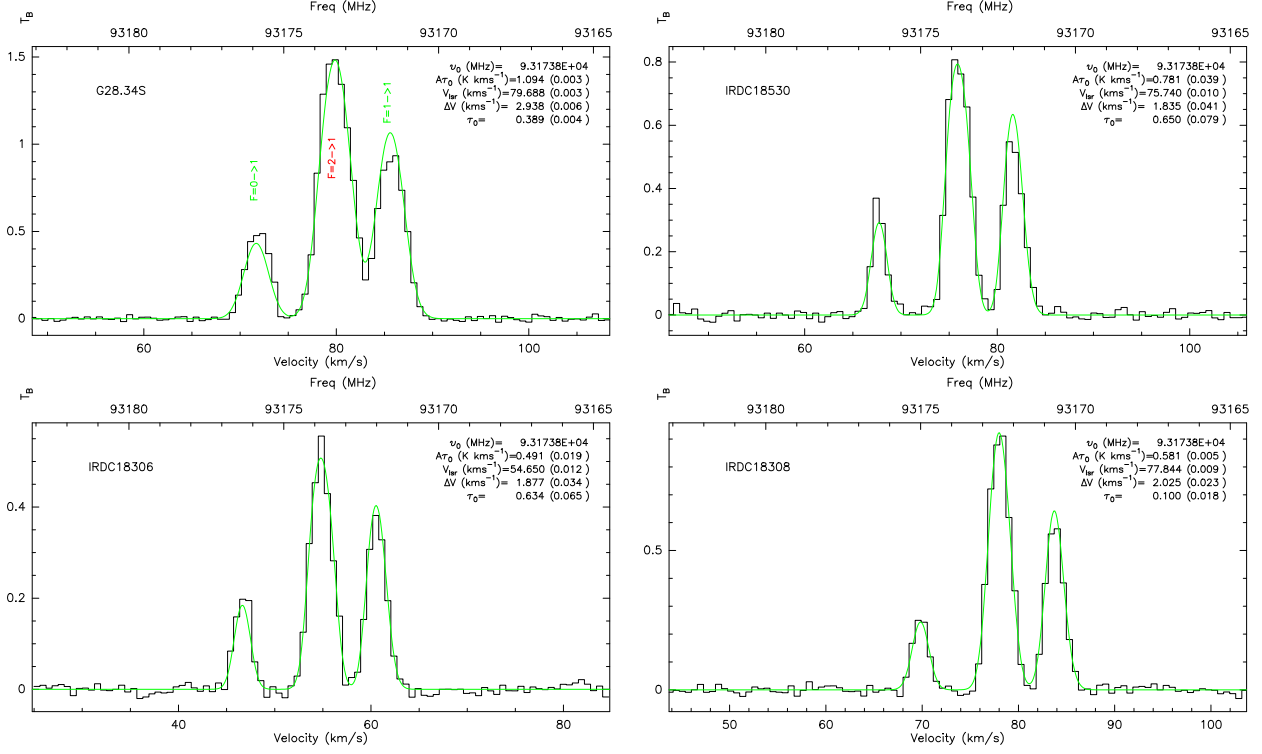
HCN ($J = 1 \rightarrow 0$) has an anomalous line profile in IRDC 18306 (the HFS component with the strongest relative intensity shows weaker emission than the others). This “anomalousness” has also been noted by Afonso et al. (1998) and was explained as the inconsistency intensity ratios between multiplets of HCN , i.e., individual hyperfine lines may be enhanced or suppressed in dark clouds because of non-LTE (Loughnane et al. 2012). Therefore, the low T_{ex} we derive here are the averaged excitation temperatures from the imperfectly fitted spectrum (Figure 5.III).

(3) The HFS method is applicable when the source is in ideal LTE (assumption ①–③ in Appendix A) and multiplets are resolved (assumption ④). However, in our observations HCN and H^{13}CN may be non-LTE, and seven multiplet lines of N_2H^+ are blended into three Gaussian peaks at a velocity resolution of $\sim 0.641 \text{ km s}^{-1}$ (Figure 5.I). Therefore, the HFS method only gives the rough level of the T_{ex} .

(4) Another factor which would affect the T_{ex} estimation is the filling factor f , which is estimated by assuming that the species emission extent is equal to the area within the contour of half maximum integrated intensity (Eq. A.1–A.3). In most cases, the emission extends over the 30 m primary beam, so $f \sim 1$. For species whose equivalent distribution diameter is smaller than the primary beam could have a $f \ll 1$ (e.g., H^{13}CN in IRDC 18306 and IRDC 18308 have $f < 0.5$). Moreover, the asymmetric spatial distribution of emission would also bring uncertainty (i.e., the equivalent distribution diameter depends on the velocity range we integrate and the edge of the emission extent we define). On average, T_{ex} is underestimated for $f \sim 1$ and will increase by a factor of 1.2–1.5 for $f \sim 0.2$.

Following the “CTex” approach introduced by Caselli et al. (2002c), where N_2H^+ with $T_{\text{ex}} \sim 5 \text{ K}$, we assume that the transitions of each molecule can be described by an approximately constant T_{ex} . Then we estimate the column densities of the above species¹⁹ with Eq. A.4.

¹⁹ A more precise approach is to use the non-LTE radiative transfer code RADEX. However, it does not significantly improve our results, when we do not know the source structure.

I. N_2H^+ ($J = 1 \rightarrow 0$)


*. Hyperfine multiplet is fitted using seven components, which are not resolvable in our data, so we label the three strongest hyperfine lines.

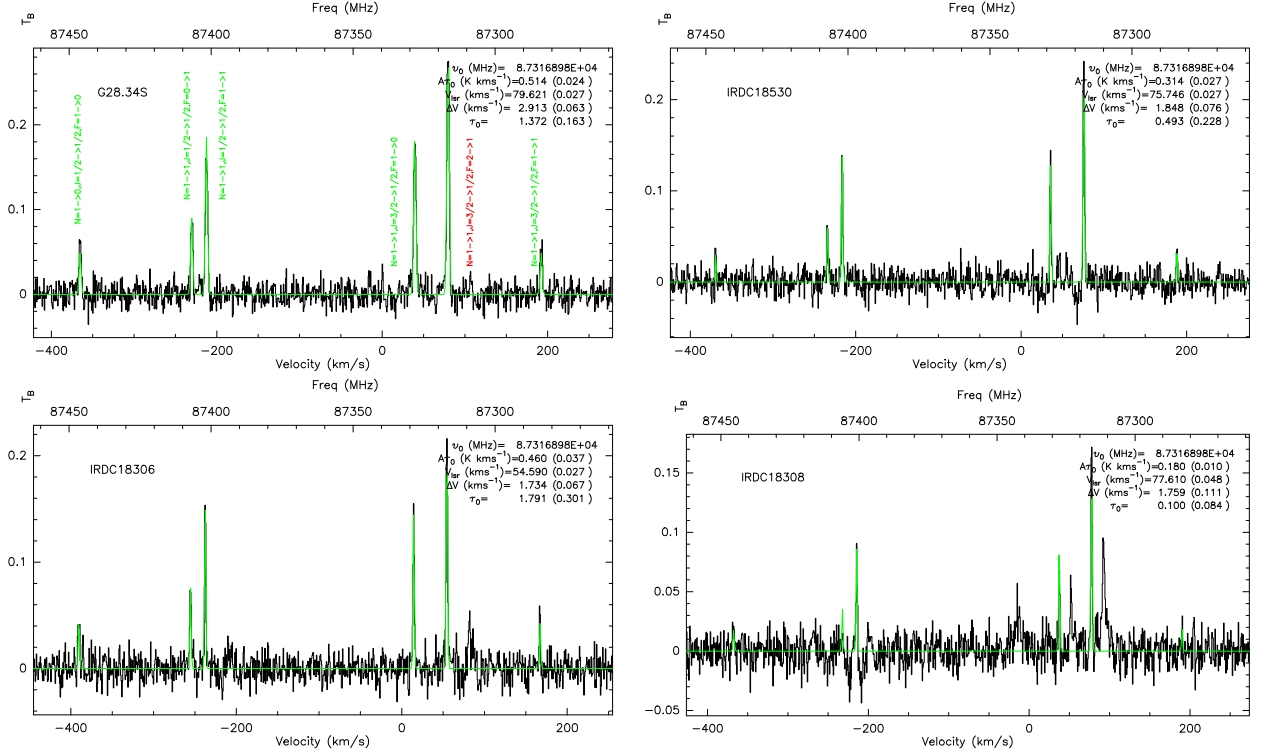
 II. C_2H ($N = 1 \rightarrow 0$)


Fig. 5: Hyperfine multiplet fits (green lines) to the observed N_2H^+ ($J = 1 \rightarrow 0$), C_2H ($N = 1 \rightarrow 0$), HCN ($J = 1 \rightarrow 0$), and H^{13}CN ($J = 1 \rightarrow 0$) (black histograms) from each IRDC; the fit parameters are in the right upper corner. The transitions of multiplets are labeled in the panels of G28.34 S (with the strongest line in red).

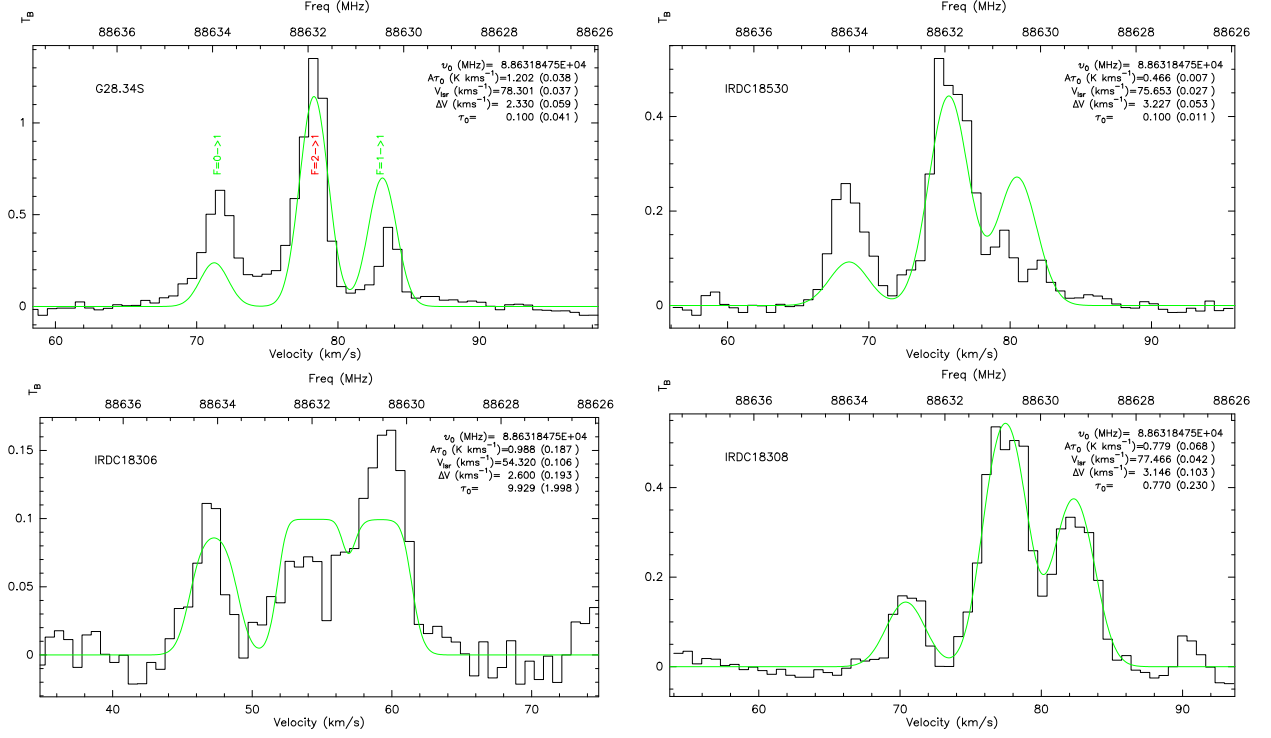
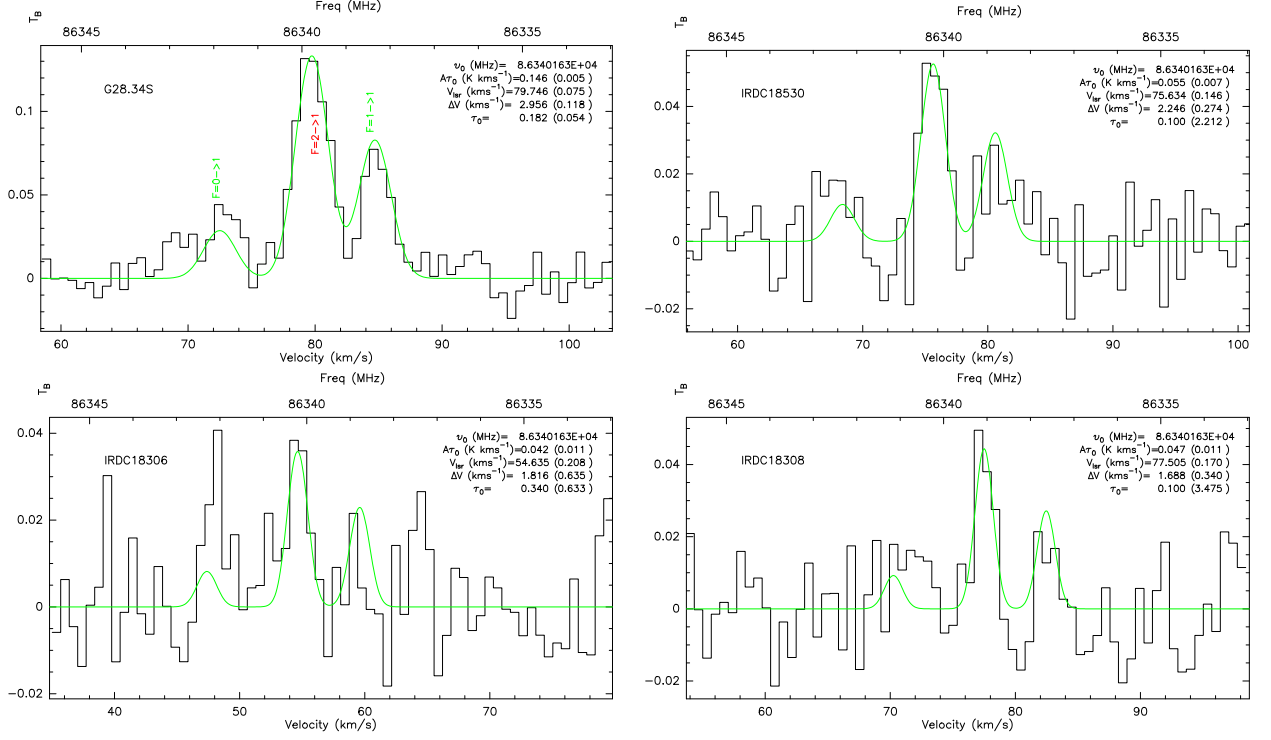
III. HCN ($J = 1 \rightarrow 0$)

 IV. H 13 CN ($J = 1 \rightarrow 0$)


Fig. 5: (continued)

– Molecules without hyperfine multiplet

CO isotopologues are important gas tracers because of their low dipole moments and thermalization near their critical densities (at 10–20 K, $\sim 10^3 \text{ cm}^{-3}$ for ^{13}CO ($2 \rightarrow 1$), $\sim 10^4 \text{ cm}^{-3}$ for C^{18}O ($2 \rightarrow 1$) and C^{17}O ($2 \rightarrow 1$)). Therefore, they are in LTE in our dense gas clumps ($n = 10^4\text{--}10^5 \text{ cm}^{-3}$), and their T_{ex} can be taken as the T_{kin} of the gas.

Lower-J transitions of the CO isotopologues (e.g., ^{13}CO ($2 \rightarrow 1$)) may be optically thick, so a precise estimation of its T_{ex} needs opacity correction. Assuming that fractionation (isotopic exchange reaction) of $^{12}\text{C} \rightleftharpoons ^{13}\text{C}$ and of $^{17}\text{O} \rightleftharpoons ^{16}\text{O} \rightleftharpoons ^{18}\text{O}$ are stable, we correct the optical depth τ and estimate T_{ex} of CO isotopologue ($1 \rightarrow 0$) lines (listed in Table 7, see Appendix B for details).

For G28.34 S and IRDC 18306, C^{18}O ($2 \rightarrow 1$) is optically thin according to our optical depth measurements from C^{17}O ($2 \rightarrow 1$) (Table 7). Since we did not observe C^{17}O ($1 \rightarrow 0$) in IRDC 18530, and the intensity of this line is only $\sim 3\sigma$ rms in IRDC 18308, we take the optically thin C^{18}O ($2 \rightarrow 1$) as a standard to estimate the other chemical parameters.

The values of T_{ex} derived from CO isotopologues are consistent in G28.34 S (11–14 K), indicating that CO is in LTE. This temperature range is also consistent with the values derived from VLA+Effelsberg NH_3 observations, the SABOCA $350 \mu\text{m}$ survey, and SPIRE $500 \mu\text{m}$ observations (mentioned in Section 4.1). Most of the other lines without hyperfine multiplets have low critical density (except for SiO ($2 \rightarrow 1$)), so we assume they are coupled with dust and thermalized at $T_{\text{gas}} = T_{\text{dust}} = T_{\text{kin}} \sim T_{\text{ex,CO}}$. The column densities of these species can be derived according to Appendix C. In particular, the column densities of species whose rare isotopologue lines we detected (HCO^+ , HNC, and ^{13}CO) are derived after opacity corrections.

Molecular column densities estimated using the above approaches are listed in Tables A4–A5.

4.3.2. H_2 column density estimates

It is possible to estimate H_2 column density at clump-scale from Eq. 3. At the temperature of $T_{\text{ATLAS}} = T_{\text{ex,CO}} \sim 10 \text{ K}$, average H_2 column density measured from the ATLASGAL in the $40'' \times 40''$ region is on the order of 10^{23} cm^{-2} (1 g cm^{-2} , Table 8), which is consistent with the threshold for high-mass star-forming clouds proposed by Krumholz & McKee (2008).

4.3.3. Molecular abundance with respect to H_2

APEX has a comparable beam size ($18''$) to the IRAM 30 m at 1 mm ($12''$) and 3 mm ($30''$). Therefore, assuming that the averaged continuum specific intensity at $18''$ angular resolution (from APEX) is comparable to that at $12''\text{--}30''$ resolution (from the 30 m), the average molecular abundances with respect to H_2 at the clump scale (within $40'' \times 40''$ region) can be estimated (Tables A4–A5). One needs to keep in mind that the difference in the beam size will lead to the overestimation of the 1 mm molecular abundance and underestimation of the 3 mm molecular abundance by a factor of 2–3 because the H_2 column density (Eq. 3) is underestimated at 1 mm and overestimated at

3 mm.

The column densities of N_2H^+ , C_2H , HCN, and H^{13}CN are estimated with respect to T_{ex} estimated from their HFS fittings. Since T_{ex} is different from that of the dust temperature used to derive the H_2 column density, it introduces a large uncertainty for the column density estimates. Previous molecular spectral line observations towards several IRDCs have shown the typical range of $T_{\text{kin}} = 10\text{--}20 \text{ K}$ (e.g., Carey et al. 1998; Teyssier et al. 2002; Sridharan et al. 2005; Pillai et al. 2006; Sakai et al. 2008; Devine et al. 2011; Ragan et al. 2011; Zhang & Wang 2011). In addition, spectral energy distributions of clumps within “quiescent” IRDCs indicate a range of dust temperature $T_{\text{dust}} = 10\text{--}30 \text{ K}$ (e.g., Henning et al. 2010; Rathborne et al. 2010). Therefore, we also estimate the column densities and abundances of N_2H^+ , C_2H , HCN, and H^{13}CN at the same $T_{\text{kin}} \sim T_{\text{ex,CO}}$ as the other species (see Table A4). Comparison between the values at these two sets of temperatures indicates that the molecular abundances are sensitive to the temperatures in the 5–15 K regime, and 5 K difference in temperature brings the abundance uncertainty to the order of 1–2 magnitudes. In the following analysis, we use the abundances at $\sim T_{\text{ex,CO}}$ to estimate the other chemical parameters.

4.4. Chemical similarity and diversity of our sample compared to other HMSCs

On the clump-core scale ($\sim 0.8 \text{ pc}$), most strong emission lines detected by the 30 m observations are from N-bearing species, which show anti-correlation spatial distribution with CO isotopologues in G28.34 S and IRDC 18308. Emissions from shock tracers (e.g., SiO in G28.34 S and HNC), infall tracers (e.g., HCO^+ and HCN), and the detection of carbon ring (e.g., $\text{c-C}_3\text{H}_2$) indicate that these cold, young clouds are not completely “quiescent”.

Although the above features are qualitatively similar to the low-mass prestellar objects (LMPO) (typical scale of $\sim 0.02 \text{ pc}$, Ohishi et al. 1992; Jørgensen et al. 2004; Tafalla et al. 2006), quantitative comparison between HMSCs and LMPOs requires observations on the same spatial scale. We compare the molecular abundances in our sources with previous spectral line studies in other HMSCs (e.g., Vasyunina et al. 2009; Gerner et al. 2014). On the one hand, all species in our sources have, on average, lower abundances than the above-mentioned studies, probably owing to our lower²⁰ T_{kin} and the possibly overestimated H_2 column density (Section 4.3.3). Therefore, a more precise estimation of the molecular abundance requires a more reliable temperature measurement. On the other hand, species have higher abundances in G28.34 S than the others in our sample, again indicating that it is a chemically more evolved source.

The typical dense gas tracers HCN and HNC are a pair of isomers whose abundance ratio is strongly temperature dependent. It has been reported that the HCN/HNC ratio decreases with increasing temperature, ranging from ≤ 1 in the low-mass prestellar cores (e.g., Ohishi et al. 1992; Jørgensen et al. 2004;

²⁰ The molecular abundance estimated in our study is, on average, one magnitude lower than the IRDC large sample study by Gerner et al. (2014). However, if we assume a higher $T_{\text{kin}} \sim 15 \text{ K}$ (as in Gerner et al. 2014), the molecular abundances are comparable.

Table 6: T_{ex} derived from hyperfine fits to N_2H^+ , C_2H , HCN, and H^{13}CN multiplets in four IRDCs

Species	G28.34 S (K)	IRDC 18530 ^a (K)	IRDC 18306 ^{a,b} (K)	IRDC 18308 ^{a,b} (K)
$\text{N}_2\text{H}^+ (J = 1 \rightarrow 0)$	5.81 ± 0.04	4.09 ± 0.21	3.62 ± 0.11	8.91 ± 0.94
$\text{C}_2\text{H} (N = 1 \rightarrow 0)$	3.14 ± 0.06	3.26 ± 0.17	3.01 ± 0.06	4.68 ± 0.98
$\text{HCN} (J = 1 \rightarrow 0)$	15.10 ± 3.81	7.70 ± 0.55	$2.82 \pm 0.04^*$	3.87 ± 0.34
$\text{H}^{13}\text{CN} (J = 1 \rightarrow 0)$	3.63 ± 0.23	$3.35 \pm 0.62^*$	$3.55 \pm 0.62^{*,\dagger}$	$5.17 \pm 2.42^{*,\dagger}$

Note. *a.* “*” denotes the fits having large deviation from the observation.

b. “†” denotes species with filling factor $f < 0.5$.

Table 7: Optical depth τ and T_{ex} derived for CO ($1 \rightarrow 0$) isotopologues, according to Eq. B.1 and B.3-B.6.

Line	G28.34 S		IRDC 18530		IRDC 18306		IRDC 18308	
	τ	T_{ex} (K)	τ	T_{ex} (K)	τ	T_{ex} (K)	τ	T_{ex} (K)
$\text{C}^{18}\text{O} (2 \rightarrow 1)^a$	0.25	14	—	—	0.65	8	—	—
$^{13}\text{CO} (2 \rightarrow 1)^a$	2.6	11	—	—	5.8	8	0.9	13
$^{13}\text{CO} (2 \rightarrow 1)^b$	2.8	11	2.9	9	6.2	7	2.2	11

Note. *a.* Derived from $\text{C}^{17}\text{O} (2 \rightarrow 1)$, which is assumed to be optically thin.

b. Derived from $\text{C}^{18}\text{O} (2 \rightarrow 1)$, which is assumed to be optically thin.

Table 8: CO depletion, HNC/HCN ratio, lower limit of ionization, and velocity asymmetric degree of H^{13}CO^+ in four IRDCs

Source	l ($^\circ$)	b ($^\circ$)	D_{GC}^a (kpc)	$I_{0.87\text{mm}}$ (Jy/beam)	T_{g} (K)	N_{H_2} 10^{22} cm^{-2}	C^{18}O	$\mathcal{D}_{\text{CO}}^b$ ^{13}CO	C^{17}O	$\text{X}(\frac{\text{HNC}}{\text{HCN}})^c$	$x(e)^e$ (10^{-7})	$\delta V_{\text{H}^{13}\text{CO}^+}^f$
G28.34 S	28.324	0.067	4.6	0.77 ± 0.10	12	13.23 ± 0.17	15.22 ± 2.19	13.71 ± 6.51	14.54 ± 2.55	1.56 ± 0.77	1.10	-0.51 ± 0.01
IRDC 18530	35.431	0.137	4.5	0.56 ± 0.07	9	17.12 ± 0.21	36.47 ± 5.24	19.54 ± 6.83	—	0.64 ± 0.22	3.66	-0.19 ± 0.002
IRDC 18306	23.296	0.056	3.6	0.48 ± 0.12	8	19.10 ± 0.48	49.81 ± 13.46	21.52 ± 6.51	41.20 ± 11.87	— ^d	6.89	0.30 ± 0.02
IRDC 18308	23.251	0.017	4.4	0.36 ± 0.07	12	6.12 ± 1.20	19.45 ± 4.31	12.16 ± 4.69	24.04 ± 7.03	— ^d	0.51	0.0009 ± 0.005

Note. *a.* Assuming the galactocentric distance of the sun is 8 kpc.

b. Estimated from C^{18}O and optical depth corrected ^{13}CO with Eqs. B.2-B.4.

c. Measured with the optical depth corrected HNC and hyperfine fitted HCN at the same gas temperature $T_{\text{ex,CO}}$.

d. The value is not given because of large uncertainties in HCN abundance, see Table A4.

e. Lower limit is measured from Eq. 17, with hyperfine fitted N_2H^+ , the optical depth corrected ^{13}CO , and H^{13}CO^+ at the same gas temperature $T_{\text{ex,CO}}$.

f. $\delta V_{\text{H}^{13}\text{CO}^+} = (V_{\text{HCO}^+} - V_{\text{H}^{13}\text{CO}^+}) / \Delta v_{\text{H}^{13}\text{CO}^+}$, Mardones et al. (1997).

Tafalla et al. 2006; Sarrasin et al. 2010) to the order of unity in dark clouds (e.g., Hirota et al. 1998; Vasyunina et al. 2011), then above 10 in high-mass protostellar objects (e.g., Blake et al. 1987; Helmich & van Dishoeck 1997), and reaching several tens in warm cores (e.g., Orion GMC, Goldsmith et al. 1986; Schilke et al. 1992). In our sources, the HCN/HNC ratio is almost unity in G28.34 S and IRDC 18530 (Table 8), which is consistent with the value in dark clouds. If we compare the abundance ratio in our study to the statistical criteria value given by Jin et al. (2015), IRDC 18530 is likely a “quiescent” IRDC, and G28.34S is more “active”.

4.5. CO depletion

The sublimation temperature of CO is around 20 K (Caselli et al. 1999; Fontani et al. 2006; Aikawa et al. 2008), so most CO is frozen out (depleted) onto the grains in the center of cold cloud. In contrast, N-bearing species are more resilient to depletion (e.g., Bergin et al. 2002; Caselli et al. 2002c; Jørgensen et al. 2004). Moreover, since CO destroys N_2H^+ and decreases the deuterium fraction, the anti-correlated spatial distribution between $\text{N}_2\text{H}^+/\text{NH}_2\text{D}$ and CO in G28.34 S and

IRDC 18308 indicates strong depletion of CO (Figure 3).

The depletion factor is defined as the ratio between the expected abundance of a species $\text{X}_\alpha^{\text{E}}$ and the observed abundance of that species $\text{X}_\alpha^{\text{O}}$ (Lacy et al., 1994), $\mathcal{D}_\alpha = \text{X}_\alpha^{\text{E}} / \text{X}_\alpha^{\text{O}}$. We measure the CO depletion factor averaged in the $40'' \times 40''$ region from $J = 2 \rightarrow 1$ lines of C^{17}O , C^{18}O , and ^{13}CO (with optical depth correction; see Table 8). Depletion factors derived from C^{17}O and C^{18}O are consistent in each IRDC (with a mean of 30). However, depletion factors derived from ^{13}CO are lower than those derived from its rare isotopologues by a factor of 2 in IRDC 18530 and IRDC 18306, indicating the canonical ratio between isotopes may have large uncertainties in both sources. One possibility is fractionation of $^{12}\text{C} \rightleftharpoons ^{13}\text{C}$ and of $^{17}\text{O} \rightleftharpoons ^{16}\text{O} \rightleftharpoons ^{18}\text{O}$ in the low temperature environment (< 10 K in both sources). Nevertheless, CO seems to be heavily depleted in our sample, with a depletion factor in the range of 14–50 at < 15 K and $n \sim 10^5 \text{ cm}^{-3}$, which is consistent with the range given by Fontani et al. (2012) from a large sample study. In particular, a depletion of ~ 14 in G28.34S is consistent with that in the nearby source G28.34 S P1 (Zhang et al. 2009). Compared with G28.34 S and IRDC 18308, IRDC 18530 and IRDC 18306 have higher CO depletion factors on scales of 0.8 pc, but they do not show significant anti-correlation distribution between

CO and $\text{N}_2\text{H}^+/\text{NH}_2\text{D}$ at the spatial resolution of 0.2–0.6 pc. Therefore, high depletion of CO may happen on smaller scales (< 0.2 pc); confirming this possibility requires higher resolution maps.

4.6. Ionization

The ionization fraction $x(e)$ in the early stage of star formation is an important indicator of the cosmic ray impact in the dense, dark clouds. Based on the assumption that gas is quasi-neutral, $x(e)$ can be simply estimated by summing up the abundance of all the molecular ions (e.g., Caselli et al. 2002c; Miettinen et al. 2009). Therefore, the ionization fraction in our sources is dominated by the abundance of N_2H^+ , and on average, at a lower limit of 10^{-8} .

In addition, based on the assumption of chemical equilibrium, $x(e)$ in dense molecular clouds can also be derived from ion-neutral reaction. Using the same method as described in Miettinen et al. (2011) and the chemical network in their Table 8, we only consider the reactions between N_2H^+ , HCO^+ , and CO (the abundance is derived from C^{18}O without any fractional reactions). The lower limit of $x(e)$ can be derived as (see also Qi et al. 2003)



$$x(e) \geq \frac{k_{15}X(\text{N}_2\text{H}^+)X(\text{CO})}{\beta_{11}X(\text{HCO}^+)}, \quad (17)$$

where the rate coefficients $\beta_{11} = 2.4 \times 10^{-7} \left(\frac{T_{\text{kin}}}{300 \text{ K}}\right)^{-0.69}$ and $k_{15} = 8.8 \times 10^{-10} \text{ cm}^3 \text{ s}^{-1}$ are adopted from UMIST database (Woodall et al. 2007).

From Table 8, we found that the lower limit of ionization rate is $\sim 10^{-7}$. This method makes some assumptions, e.g., CO depletion and fractional reaction are not considered, as discussed in Caselli et al. (1998); Lintott & Rawlings (2006); Miettinen et al. (2011). Nevertheless, these more precise, model-based estimations are consistent with those reported in HMSCs (e.g., Williams et al. 1998; Bergin et al. 1999; Chen et al. 2010; Miettinen et al. 2011) and the modeling result in Gerner et al. (2014). Moreover, the lower limit of ionization rate in our large-scale (~ 0.8 pc) HMSC envelopes is higher than the model-predicted values in the center of the low-mass prestellar objects (e.g., $> 10^{-9}$, Caselli et al. 2002c). This is reasonable because the cosmic ray ionization rates in the envelope of HMSCs are higher than in the inner region of their low-mass counterparts. It is also possible that these HMSCs are in a much more active environment than low-mass prestellar cores, and hence they are affected by much more radiation of any kind.

In addition, as mentioned in Section 3.2.2, H^{13}CO^+ is “deficient” in regions where ^{13}CO is abundant in IRDC 18530. This can be explained by Eqs. 15–16, which show that the rate coefficient β_{11} is enhanced in this source.

5. Conclusions

To investigate the initial conditions of high-mass star formation, we carried out several observations with the SMA and IRAM

30 m. In this paper, we study the dynamic and chemical properties of four IRDCs (G28.34S, IRDC 18530, IRDC 18306, and IRDC 18308), which exhibit strong (sub)mm continuum emission toward 70 μm extinction features. At different spatial resolutions and wavelengths, this small sample study of IRDCs illustrates that the cold ($T < 15$ K), dense ($\sim 10^5 \text{ cm}^{-3}$) high-mass star-forming regions are not completely quiescent.

Our conclusions are as follows:

1. At an angular resolution of $2''$ ($\sim 10^4$ AU at an average distance of 4 kpc), the 1.1 mm SMA observations resolve each source into several fragments. The average separation between the fragments is 0.07–0.24 pc, comparable to the Jeans length. However, the mass of each fragment is on average $> 10 M_{\odot}$, exceeding the thermal Jeans mass of the entire clump by a factor of up to 30, indicating that thermal pressure alone does not dominate the fragmentation process.
2. In the 8 GHz SMA observational band at 1.1 mm, higher-J transitions (including dense gas tracers such as H^{13}CO^+ ($2 \rightarrow 1$)) are not detected, implying that our sources are in the cold and young evolutionary status when lines with $E_u/k_B > 20$ K may not be excited. However, our line survey at 1 mm/3 mm shows a number of emissions from lower-J transitions. In particular, a $> 5\sigma$ rms detection of SiO ($2 \rightarrow 1$) with broad line wings in G28.34 S may be the signature of a potential protostellar object, and the asymmetric HCO^+ line profile in this source traces potential infall motion at a speed of $\sim 0.84 \text{ km s}^{-1}$.
3. Linewidths of all the 30 m detected lines are on average 2–3 km s^{-1} . Using the H^{13}CO^+ ($1 \rightarrow 0$) line, we calculate the velocity dispersion components and the critical mass based on a non-thermal fragmentation scenario. Non-thermal motions can provide sufficient extra support to increase the scale of the fragmentation, making it possible to support fragments up to several hundreds of M_{\odot} against gravity. Alternative explanations may include magnetic fields and steep core density profiles. The mass of the well-aligned fragments in filament G28.34 S and IRDC 18308 is also in rough agreement with the scenario of “cylindrical fragmentation”.
4. N_2H^+ ($J = 1 \rightarrow 0$), C_2H ($N = 1 \rightarrow 0$), HCN ($J = 1 \rightarrow 0$), and H^{13}CN ($J = 1 \rightarrow 0$) have multiplets in our 30 m data. Using a hyperfine multiplet fit program, we estimate their excitation temperature (on average 5–8 K) and conclude that they are subthermally excited. The excitation temperatures of the CO isotopologues suggest that the sources are in the very early cold phase (~ 10 K).
5. Our large-scale high-mass clumps exhibit chemical features that are qualitatively similar to low-mass prestellar cores on small scales, including a large number of N-bearing species and the detection of carbon rings and molecular ions. Moreover, G28.34 S and IRDC 18308 show anti-correlated spatial distributions between $\text{N}_2\text{H}^+/\text{NH}_2\text{D}$ and CO on a scale of 0.5 pc. We calculate the molecular abundances, HCN/HNC ratio, CO depletion factor, and ionization fraction and find that G28.34 S is slightly more chemically evolved than the other sources in our sample.

6. Large-scale line surveys measure the chemical features of the high-mass clumps hosting HMSCs, but are not sufficient to probe the chemical complexity of the fragments themselves. The above observations reveal non-thermal motions, which dominate the fragmentation process from the dark cloud to the high-mass cores. However, without line detection, we do not know the dynamics within these cores. Further studies are expected to uncover the chemical and dynamic features within the densest fragments of IRDCs.

Acknowledgements. We would like to thank the SMA staff and IRAM 30 m staff for their helpful support during the reduction of the SMA data and the performance of the IRAM 30 m observations in service mode. We thank J. Pineda, Y. Wang, Z. Y. Zhang, and K. Wang for helpful discussions. We thank the anonymous reviewer for the constructive comments.

This research made use of NASA's Astrophysics Data System.

The Submillimeter Array is a joint project between the Smithsonian Astrophysical Observatory and the Academia Sinica Institute of Astronomy and Astrophysics and is funded by the Smithsonian Institution and the Academia Sinica.

References

- Afonso, J. M., Yun, J. L., & Clemens, D. P. 1998, *AJ*, 115, 1111
- Aikawa, Y., Wakelam, V., Garrod, R. T., & Herbst, E. 2008, *ApJ*, 674, 984
- Bastien, P., Arcoragi, J.-P., Benz, W., Bonnell, I., & Martel, H. 1991, *ApJ*, 378, 255
- Bergin, E. A. 2003, in *SFChem 2002: Chemistry as a Diagnostic of Star Formation*, ed. C. L. Curry & M. Fich, 63
- Bergin, E. A., Alves, J., Huard, T., & Lada, C. J. 2002, *ApJ*, 570, L101
- Bergin, E. A., Goldsmith, P. F., Snell, R. L., & Ungerechts, H. 1994, *ApJ*, 431, 674
- Bergin, E. A., Plume, R., Williams, J. P., & Myers, P. C. 1999, *ApJ*, 512, 724
- Bergin, E. A., Snell, R. L., & Goldsmith, P. F. 1996, *ApJ*, 460, 343
- Bergin, E. A. & Tafalla, M. 2007, *ARA&A*, 45, 339
- Beuther, H. & Henning, T. 2009, *A&A*, 503, 859
- Beuther, H., Henning, T., Linz, H., et al. 2015, *A&A*, 581, A119
- Beuther, H., Henning, T., Linz, H., et al. 2010, *A&A*, 518, L78
- Beuther, H., Kainulainen, J., Henning, T., Plume, R., & Heitsch, F. 2011, *A&A*, 533, A17
- Beuther, H., Linz, H., Tackenberg, J., et al. 2013, *A&A*, 553, A115
- Beuther, H., Schilke, P., Menten, K. M., et al. 2002, *ApJ*, 566, 945
- Beuther, H., Semenov, D., Henning, T., & Linz, H. 2008, *ApJ*, 675, L33
- Beuther, H. & Sridharan, T. K. 2007, *ApJ*, 668, 348
- Beuther, H., Tackenberg, J., Linz, H., et al. 2012, *A&A*, 538, A11
- Beuther, H., Zhang, Q., Bergin, E. A., & Sridharan, T. K. 2009, *AJ*, 137, 406
- Bühr, S., Beuther, H., Linz, H., et al. 2015, *A&A*, 579, A51
- Blake, G. A., Sutton, E. C., Masson, C. R., & Phillips, T. G. 1987, *ApJ*, 315, 621
- Bontemps, S., Motte, F., Csengeri, T., & Schneider, N. 2010, *A&A*, 524, A18
- Bronfman, L., Nyman, L.-A., & May, J. 1996, *A&AS*, 115, 81
- Butler, M. J. & Tan, J. C. 2009, *ApJ*, 696, 484
- Carey, S. J., Clark, F. O., Egan, M. P., et al. 1998, *ApJ*, 508, 721
- Caselli, P., Benson, P. J., Myers, P. C., & Tafalla, M. 2002a, *ApJ*, 572, 238
- Caselli, P., Walmsley, C. M., Tafalla, M., Dore, L., & Myers, P. C. 1999, *ApJ*, 523, L165
- Caselli, P., Walmsley, C. M., Terzieva, R., & Herbst, E. 1998, *ApJ*, 499, 234
- Caselli, P., Walmsley, C. M., Zucconi, A., et al. 2002b, *ApJ*, 565, 331
- Caselli, P., Walmsley, C. M., Zucconi, A., et al. 2002c, *ApJ*, 565, 344
- Chambers, E. T., Jackson, J. M., Rathborne, J. M., & Simon, R. 2009, *ApJS*, 181, 360
- Chandrasekhar, S. & Fermi, E. 1953, *ApJ*, 118, 116
- Chen, H.-R., Liu, S.-Y., Su, Y.-N., & Zhang, Q. 2010, *ApJ*, 713, L50
- Chin, Y.-N., Henkel, C., Whiteoak, J. B., Langer, N., & Churchwell, E. B. 1996, *A&A*, 305, 960
- Chira, R.-A., Beuther, H., Linz, H., et al. 2013, *A&A*, 552, A40
- Codella, C., Bachiller, R., Nisini, B., Saraceno, P., & Testi, L. 2001, *A&A*, 376, 271
- Commerçon, B., Hennebelle, P., & Henning, T. 2011, *ApJ*, 742, L9
- Crapsi, A., Caselli, P., Walmsley, C. M., et al. 2005, *ApJ*, 619, 379
- Csengeri, T., Bontemps, S., Schneider, N., Motte, F., & Dib, S. 2011, *A&A*, 527, A135
- Devine, K. E., Chandler, C. J., Brogan, C., et al. 2011, *ApJ*, 733, 44
- Dobbs, C. L., Bonnell, I. A., & Clark, P. C. 2005, *MNRAS*, 360, 2
- Draine, B. T. 2011, *Physics of the Interstellar and Intergalactic Medium*
- Feng, S., Beuther, H., Semenov, D., et al. 2016, *ArXiv e-prints*
- Fiege, J. D. & Pudritz, R. E. 2000, *MNRAS*, 311, 85
- Fischera, J. & Martin, P. G. 2012, *A&A*, 542, A77
- Fontani, F., Caselli, P., Crapsi, A., et al. 2006, *A&A*, 460, 709
- Fontani, F., Giannetti, A., Beltrán, M. T., et al. 2012, *MNRAS*, 423, 2342
- Fontani, F., Sakai, T., Furuya, K., et al. 2014, *MNRAS*, 440, 448
- Frerking, M. A., Langer, W. D., & Wilson, R. W. 1982, *ApJ*, 262, 590
- Fuller, G. A., Williams, S. J., & Sridharan, T. K. 2005, *A&A*, 442, 949
- Garrod, R. T., Weaver, S. L. W., & Herbst, E. 2008, *ApJ*, 682, 283
- Gerner, T., Beuther, H., Semenov, D., et al. 2014, *A&A*, 563, A97
- Giannetti, A., Wyrowski, F., Brand, J., et al. 2014, *A&A*, 570, A65
- Girichidis, P., Federrath, C., Banerjee, R., & Klessen, R. S. 2011, *MNRAS*, 413, 2741
- Goldsmith, P. F., Irvine, W. M., Hjalmarson, A., & Ellender, J. 1986, *ApJ*, 310, 383
- Goodman, A. A., Benson, P. J., Fuller, G. A., & Myers, P. C. 1993, *ApJ*, 406, 528
- Helmich, F. P. & van Dishoeck, E. F. 1997, *A&AS*, 124, 205
- Henning, T., Linz, H., Krause, O., et al. 2010, *A&A*, 518, L95
- Hildebrand, R. H. 1983, *QJRAS*, 24, 267
- Hirota, T., Yamamoto, S., Mikami, H., & Ohishi, M. 1998, *ApJ*, 503, 717
- Ho, P. T. P., Moran, J. M., & Lo, K. Y. 2004, *ApJ*, 616, L1
- Hofner, P., Wiesemeyer, H., & Henning, T. 2001, *ApJ*, 549, 425
- Horn, A., Möllendal, H., Sekiguchi, O., et al. 2004, *ApJ*, 611, 605
- Inutsuka, S.-I. & Miyama, S. M. 1992, *ApJ*, 388, 392
- Jackson, J. M., Finn, S. C., Chambers, E. T., Rathborne, J. M., & Simon, R. 2010, *ApJ*, 719, L185
- Jiménez-Serra, I., Caselli, P., Tan, J. C., et al. 2010, *MNRAS*, 406, 187
- Jiménez-Serra, I., Martín-Pintado, J., Caselli, P., Viti, S., & Rodríguez-Franco, A. 2009, *ApJ*, 695, 149
- Jin, M., Lee, J.-E., & Kim, K.-T. 2015, *ApJS*, 219, 2
- Jones, P. A., Burton, M. G., Cunningham, M. R., et al. 2008, *MNRAS*, 386, 117
- Jørgensen, J. K., Schöier, F. L., & van Dishoeck, E. F. 2004, *A&A*, 416, 603
- Kainulainen, J., Ragan, S. E., Henning, T., & Stutz, A. 2013, *A&A*, 557, A120
- Kirk, H., Johnstone, D., & Di Francesco, J. 2006, *ApJ*, 646, 1009
- Kirk, H., Klassen, M., Pudritz, R., & Pillsworth, S. 2015, *ApJ*, 802, 75
- Krumholz, M. R. & McKee, C. F. 2008, *Nature*, 451, 1082
- Lee, C. W., Myers, P. C., & Tafalla, M. 2001, *ApJS*, 136, 703
- Lintott, C. J. & Rawlings, J. M. C. 2006, *A&A*, 448, 425
- Linz, H., Krause, O., Beuther, H., et al. 2010, *A&A*, 518, L123
- Loughane, R. M., Redman, M. P., Thompson, M. A., et al. 2012, *MNRAS*, 420, 1367
- Lovas, F. J. 2004, *Phys. Chem. Ref.*, 33, 117
- Mardones, D., Myers, P. C., Tafalla, M., et al. 1997, *ApJ*, 489, 719
- Maret, S., Hily-Blant, P., Pety, J., Bardeau, S., & Reynier, E. 2011, *A&A*, 526, A47
- Matthews, H. E. & Irvine, W. M. 1985, *ApJ*, 298, L61
- Meier, D. S. & Turner, J. L. 2005, *ApJ*, 618, 259
- Miettinen, O., Harju, J., Haikala, L. K., Kainulainen, J., & Johansson, L. E. B. 2009, *A&A*, 500, 845
- Miettinen, O., Hennemann, M., & Linz, H. 2011, *A&A*, 534, A134
- Motte, F., Bontemps, S., Schilke, P., et al. 2007, *A&A*, 476, 1243
- Müller, H. S. P., Schlöder, F., Stutzki, J., & Winnewisser, G. 2005, *Journal of Molecular Structure*, 742, 215
- Myers, P. C., Linke, R. A., & Benson, P. J. 1983, *ApJ*, 264, 517
- Myers, P. C., Mardones, D., Tafalla, M., Williams, J. P., & Wilner, D. J. 1996, *ApJ*, 465, L133
- Nagasawa, M. 1987, *Progress of Theoretical Physics*, 77, 635
- Nguyen-Lu'o'ng, Q., Motte, F., Carlhoff, P., et al. 2013, *ApJ*, 775, 88
- Ohishi, M., Irvine, W. M., & Kaifu, N. 1992, in *IAU Symposium, Vol. 150, Astrochemistry of Cosmic Phenomena*, ed. P. D. Singh, 171
- Ossenkopf, V. & Henning, T. 1994, *A&A*, 291, 943
- Palau, A., Rizzo, J. R., Girart, J. M., & Henkel, C. 2014, *ApJ*, 784, L21
- Palumbo, M. E., Geballe, T. R., & Tielens, A. G. G. M. 1997, *ApJ*, 479, 839
- Pickett, H. M., Poynter, R. L., Cohen, E. A., et al. 1998, *J. Quant. Spec. Radiat. Transf.*, 60, 883
- Pillai, T., Kauffmann, J., Wyrowski, F., et al. 2011, *A&A*, 530, A118
- Pillai, T., Wyrowski, F., Carey, S. J., & Menten, K. M. 2006, *A&A*, 450, 569
- Pineda, J. E., Caselli, P., & Goodman, A. A. 2008, *ApJ*, 679, 481
- Pirogov, L., Zinchenko, I., Caselli, P., Johansson, L. E. B., & Myers, P. C. 2003, *A&A*, 405, 639
- Qi, C., Kessler, J. E., Koerner, D. W., Sargent, A. I., & Blake, G. A. 2003, *ApJ*, 597, 986
- Ragan, S., Henning, T., Krause, O., et al. 2012a, *A&A*, 547, A49
- Ragan, S. E., Bergin, E. A., & Gutermuth, R. A. 2009, *ApJ*, 698, 324
- Ragan, S. E., Bergin, E. A., Plume, R., et al. 2006, *ApJS*, 166, 567
- Ragan, S. E., Bergin, E. A., & Wilner, D. 2011, *ApJ*, 736, 163
- Ragan, S. E., Heitsch, F., Bergin, E. A., & Wilner, D. 2012b, *ApJ*, 746, 174
- Ragan, S. E., Henning, T., & Beuther, H. 2013, *A&A*, 559, A79
- Rathborne, J. M., Jackson, J. M., Chambers, E. T., et al. 2010, *ApJ*, 715, 310

- Rathborne, J. M., Jackson, J. M., & Simon, R. 2006, *ApJ*, 641, 389
- Rawlings, J. M. C., Redman, M. P., Keto, E., & Williams, D. A. 2004, *MNRAS*, 351, 1054
- Rawlings, J. M. C., Taylor, S. D., & Williams, D. A. 2000, *MNRAS*, 313, 461
- Russeil, D., Zavagno, A., Motte, F., et al. 2010, *A&A*, 515, A55
- Sakai, T., Sakai, N., Kamegai, K., et al. 2008, *ApJ*, 678, 1049
- Sanhueza, P., Jackson, J. M., Foster, J. B., et al. 2012, *ApJ*, 756, 60
- Sarrasin, E., Abdallah, D. B., Wernli, M., et al. 2010, *MNRAS*, 404, 518
- Sault, R. J., Teuben, P. J., & Wright, M. C. H. 1995, in *Astronomical Society of the Pacific Conference Series*, Vol. 77, *Astronomical Data Analysis Software and Systems IV*, ed. R. A. Shaw, H. E. Payne, & J. J. E. Hayes, 433
- Schilke, P., Walmsley, C. M., Pineau Des Forets, G., et al. 1992, *A&A*, 256, 595
- Schuller, F., Menten, K. M., Contreras, Y., et al. 2009, *A&A*, 504, 415
- Shirley, Y. L. 2015, *PASP*, 127, 299
- Sohn, J., Lee, C. W., Park, Y.-S., et al. 2007, *ApJ*, 664, 928
- Sridharan, T. K., Beuther, H., Saito, M., Wyrowski, F., & Schilke, P. 2005, *ApJ*, 634, L57
- Tackenberg, J., Beuther, H., Henning, T., et al. 2012, *A&A*, 540, A113
- Tafalla, M., Mardones, D., Myers, P. C., et al. 1998, *ApJ*, 504, 900
- Tafalla, M., Myers, P. C., Caselli, P., Walmsley, C. M., & Comito, C. 2002, *ApJ*, 569, 815
- Tafalla, M., Santiago-García, J., Myers, P. C., et al. 2006, *A&A*, 455, 577
- Teyssier, D., Hennebelle, P., & Pérou, M. 2002, *A&A*, 382, 624
- Vasyunina, T., Linz, H., Henning, T., et al. 2009, *A&A*, 499, 149
- Vasyunina, T., Linz, H., Henning, T., et al. 2011, *A&A*, 527, A88
- Walawender, J., Bally, J., Kirk, H., & Johnstone, D. 2005, *AJ*, 130, 1795
- Wang, K., Testi, L., Ginsburg, A., et al. 2015, *MNRAS*, 450, 4043
- Wang, K., Zhang, Q., Testi, L., et al. 2014, *MNRAS*, 439, 3275
- Wang, K., Zhang, Q., Wu, Y., & Zhang, H. 2011, *ApJ*, 735, 64
- Wang, Y., Zhang, Q., Pillai, T., Wyrowski, F., & Wu, Y. 2008, *ApJ*, 672, L33
- Wang, Y., Zhang, Q., Rathborne, J. M., Jackson, J., & Wu, Y. 2006, *ApJ*, 651, L125
- Wienen, M., Wyrowski, F., Schuller, F., et al. 2012, *A&A*, 544, A146
- Williams, J. P., Bergin, E. A., Caselli, P., Myers, P. C., & Plume, R. 1998, *ApJ*, 503, 689
- Wilson, T. L. & Rood, R. 1994, *ARA&A*, 32, 191
- Woodall, J., Agúndez, M., Markwick-Kemper, A. J., & Millar, T. J. 2007, *A&A*, 466, 1197
- Wu, J., Evans, II, N. J., Shirley, Y. L., & Knez, C. 2010, *ApJS*, 188, 313
- Zhang, Q. & Wang, K. 2011, *ApJ*, 733, 26
- Zhang, Q., Wang, K., Lu, X., & Jiménez-Serra, I. 2015, *ApJ*, 804, 141
- Zhang, Q., Wang, Y., Pillai, T., & Rathborne, J. 2009, *ApJ*, 696, 268
- Zinchenko, I., Henkel, C., & Mao, R. Q. 2000, *A&A*, 361, 1079

Appendix A: Molecular column density based on the HFS fit

The HFS method is based on the CLASS software package. In the fit model, the relative intensities with respect to the reference line (we set it as the strongest one) are converted from the $\ell(300\text{K})$ value in the Splatalogue database.

Four assumptions are made in the HFS fit for one species:

- ① All the components of the multiplet have the same excitation temperature.
- ② The lines and their optical depths have Gaussian profiles.
- ③ All the multiplets have the same linewidth.
- ④ The multiplet components do not overlap.

One important parameter is the beam filling factor f . Although the distributions of most species are much more extended than the 30 m primary beam, the emission extents of some species (e.g., H^{13}CN in IRDC 18306 and IRDC 18308) are smaller than the beam. To estimate the filling factor (on the first order), we define an equivalent angular diameter of the emission extent θ_{mol} as (Wu et al. 2010)

$$\theta_{\text{mol}} = 2\left(\frac{\mathcal{A}_{1/2}}{\pi} - \frac{\theta_{30\text{m}}^2}{4}\right)^{1/2} \quad (\text{rad}), \quad (\text{A.1})$$

where $\mathcal{A}_{1/2}$ is molecular extent within the contour of half maximum integrated intensity and $\theta_{30\text{m}}$ is the primary beam of 30 m at the molecular rest frequency.

With the beam filling factor $f = \theta_{\text{mol}}^2/(\theta_{\text{mol}}^2 + \theta_{30\text{m}}^2)$, background radiation temperature T_{bg} (assumed to be 2.7 K), and the intensity in units of temperature $J_{\nu}(T) = (h\nu/k_B)/[\exp(h\nu/k_B T) - 1]$, this method defines an effective intensity A as

$$A = f[J_{\nu}(T_{\text{ex}}) - J_{\nu}(T_{\text{bg}})] \quad (\text{K}). \quad (\text{A.2})$$

The output parameters are V_{lfr} , the optical depth τ_0 , the linewidth $\Delta\nu$, and the value of effective intensity affected by the line optical depth $A\tau_0$ of the reference line. Therefore, with the light speed c , the Planck constant h , and a constant factor $\eta = 2.7964 \times 10^{-16}$ derived from Pickett et al. (1998), the excitation temperature of the multiplet T_{ex} and the molecular column density $N_{T,\alpha}$ at the frequency ν (in Hz) are given as

$$T_{\text{ex}} = \frac{h\nu/k_B}{\ln\left[\frac{h\nu/k_B}{A/f + J_{\nu}(T_{\text{bg}})} + 1\right]} \quad (\text{K}) \quad (\text{A.3})$$

$$N_{T,\alpha} = \frac{8\pi\nu}{\ell(T_{\text{ex}})\eta c^3} \tau_0 \Delta\nu \quad (\text{cm}^{-2}) \quad (\text{A.4})$$

Appendix B: Opacities and excitation temperatures of CO isotopologue lines

^{13}CO ($2 \rightarrow 1$), C^{18}O ($2 \rightarrow 1$), and C^{17}O ($2 \rightarrow 1$) are all detected in our data. To estimate their excitation temperatures, we need to know their optical depths. Assuming that fractionation (isotopic exchange reaction) of $^{12}\text{C} \rightleftharpoons ^{13}\text{C}$ and of $^{17}\text{O} \rightleftharpoons ^{16}\text{O} \rightleftharpoons ^{18}\text{O}$ are stable, we can estimate the optical depth at the line center of a given transition $\tau_{\alpha,0}$ by measuring the ratio between the main beam brightness temperature of the main line $T_{\text{mb},\alpha,0}$ and its isotopologue $T_{\text{mb},\beta,0}$, (Myers et al. 1983):

$$\frac{1 - \exp(-\tau_{\alpha,0}/\mathfrak{R}_\alpha)}{1 - \exp(-\tau_{\alpha,0})} \approx \frac{T_{\text{mb},\beta,0}}{T_{\text{mb},\alpha,0}}. \quad (\text{B.1})$$

Here \mathfrak{R}_α is the intrinsic abundance of the main isotope (e.g., ^{12}C) compared to its rare isotope (e.g., ^{13}C) in the ISM (e.g., Wilson & Rood 1994; Chin et al. 1996).

Since the line profiles of CO isotopologues in our sample are contributions from various Galactic arms (Beuther & Sridharan 2007), we use a multi-Gaussian profile to fit their T_{mb} . Then, assuming that C^{17}O ($2 \rightarrow 1$) is optically thin and that all the lines are in LTE, we use Eq. B.1 and the canonical ratio between isotopes (the following Eq. B.3-B.5, Frerking et al. 1982; Wilson & Rood 1994; Giannetti et al. 2014) to correct the optical depth of ^{13}CO ($2 \rightarrow 1$) and C^{18}O ($2 \rightarrow 1$).

$$X_{\text{CO}}^{\text{E}} = 9.5 \times 10^{-5} \exp(1.105 - 0.13 D_{\text{GC}}) \quad (\text{B.2})$$

$$\mathfrak{R}_{^{12}\text{C}/^{13}\text{C}}^{\text{E}} = 7.5 D_{\text{GC}} + 7.6 \quad (\text{B.3})$$

$$\mathfrak{R}_{^{16}\text{O}/^{18}\text{O}}^{\text{E}} = 58.8 D_{\text{GC}} + 37.1 \quad (\text{B.4})$$

$$\mathfrak{R}_{^{16}\text{O}/^{17}\text{O}}^{\text{E}} = 3.52 \times (58.8 D_{\text{GC}} + 37.1) \quad (\text{B.5})$$

where D_{GC} (kpc) is the galactic center distance, and X_α^{E} is the canonical (undepleted) abundance of isotopologue α with respect to H_2 .

Subsequently, using Eq. B.6, we estimate T_{ex} of each CO isotopologue (see Table 7):

$$T_{\text{ex}} = \frac{h\nu_\alpha/k_{\text{B}}}{\ln\left[\frac{h\nu_\alpha/k_{\text{B}}}{T_{\text{mb},\alpha,0}/(1-e^{-\tau_\alpha}) + J_\alpha(T_{\text{bg}})} + 1\right]} \quad (\text{K}) \quad (\text{B.6})$$

Appendix C: Molecular column densities for species without hyperfine multiplets

Consistent T_{ex} of CO isotopologues (Table 7) indicates they are in LTE. Since most of the other lines without hyperfine multiplets have low critical density (except for SiO ($2 \rightarrow 1$)), we assume they are coupled with dust and thermalized at $T_{\text{gas}} = T_{\text{dust}} = T_{\text{kin}} \sim T_{\text{ex,CO}}$. The column densities of these species can be derived as

$$N_{\text{T},\alpha} = \frac{k_{\text{B}}}{hcf} \frac{(e^{\frac{h\nu}{k_{\text{B}} T_{\text{ex,CO}}}} - 1)}{\ell(T_{\text{ex,CO}})} T_{\text{ex,CO}} \int \tau_\nu d\nu \quad (\text{cm}^{-2}). \quad (\text{C.1})$$

Assuming that the observed emission homogeneously distributes in the primary beam of 30 m, the integration of measured main beam brightness temperature within the velocity range $\int T_{\text{mb}}(\nu) d\nu$ can be substituted for the last term in the above equation:

$$T_{\text{ex,CO}} \int \tau_\nu d\nu \cong \frac{\tau_{\alpha,0}}{1 - e^{-\tau_{\alpha,0}}} \int T_{\text{mb}}(\nu) d\nu \quad (\text{K km s}^{-1}). \quad (\text{C.2})$$

(1) For species with neither a hyperfine multiplet nor a rare isotopologue, we assume they are optically thin, therefore,

$\frac{\tau_{\alpha,0}}{1 - e^{-\tau_{\alpha,0}}} \sim 1$.
(2) HCO^+ , HNC, and ^{13}CO : ^{13}CO ($2 \rightarrow 1$) is optically thick in at least two of our sources when measured with C^{17}O ($2 \rightarrow 1$), and the other lines may have the same issue. As we have the rare isotopologues of HCO^+ ($1 \rightarrow 0$) and

HNC ($1 \rightarrow 0$) in our data, we use Eq. B.1 to obtain their optical depths and correct their column densities by assuming that both H^{13}CO^+ ($1 \rightarrow 0$) and HN^{13}C ($1 \rightarrow 0$) are optically thin.

In sources where the emission of species $\leq 3\sigma$ rms, we give their column density upper limit by assuming that f is unity.

Table A1: Identified lines from the 30 m line survey in G28.34 S; the lines detected only in the “extra band” are in blue. Lines are imaged in Figure 3.

Freq. (MHz)	Mol.	Transition	$\ell(300\text{K})$	$S\mu^2$ (D ²)	E_l (cm)	E_u/k (K)
85139.103	OCS	$J = 7 \rightarrow 6$	-3.79540	3.58037	8.51990	16.34417
85338.894	c-C ₃ H ₂	$2_{1,2} \rightarrow 1_{0,1}$	-3.74410	48.14839	1.63320	6.44539
85455.667	CH ₃ C ₂ H	$5_1 \rightarrow 4_1$	-4.81870	1.79654	10.72420	19.53084
85457.300	CH ₃ C ₂ H	$5_0 \rightarrow 4_0$	-4.79050	1.87136	5.70120	12.30399
85926.278	NH ₂ D	$1_{1,1,0s} \rightarrow 1_{0,1,0a}$	-3.45800	28.59712	11.50630	20.67869
86338.733	H ¹³ CN	$J = 1 \rightarrow 0, F = 1 \rightarrow 1$	-3.02460	8.91106	0.00000	4.14358
86340.163	H ¹³ CN	$J = 1 \rightarrow 0, F = 2 \rightarrow 1$	-2.80270	14.85302	0.00000	4.14365
86342.251	H ¹³ CN	$J = 1 \rightarrow 0, F = 0 \rightarrow 1$	-3.50170	2.97026	0.00000	4.14375
86754.288	H ¹³ CO ⁺	$J = 1 \rightarrow 0$	-2.28080	15.21089	0.00000	4.16353
86846.960	SiO	$J = 2 \rightarrow 1$	-2.48320	19.19714	1.44850	6.25203
87090.850	HN ¹³ C	$J = 1 \rightarrow 0$	-2.59520	7.28184	0.00000	4.17968
87284.105	C ₂ H	$N = 1 \rightarrow 0, J = 3/2 \rightarrow 1/2, F = 1 \rightarrow 1$	-5.18050	0.10046	0.00150	4.19111
87316.898	C ₂ H	$N = 1 \rightarrow 0, J = 3/2 \rightarrow 1/2, F = 2 \rightarrow 1$	-4.18850	0.98557	0.00150	4.19268
87328.585	C ₂ H	$N = 1 \rightarrow 0, J = 3/2 \rightarrow 1/2, F = 1 \rightarrow 0$	-4.49110	0.49087	0.00000	4.19109
87401.989	C ₂ H	$N = 1 \rightarrow 0, J = 1/2 \rightarrow 1/2, F = 1 \rightarrow 1$	-4.49040	0.49084	0.00150	4.19677
87407.165	C ₂ H	$N = 1 \rightarrow 0, J = 1/2 \rightarrow 1/2, F = 0 \rightarrow 1$	-4.88650	0.19715	0.00150	4.19702
87446.470	C ₂ H	$N = 1 \rightarrow 0, J = 1/2 \rightarrow 1/2, F = 1 \rightarrow 0$	-5.17890	0.10046	0.00000	4.19674
87925.237	HNCO	$4_{0,4} \rightarrow 3_{0,3}$	-3.73180	9.98656	4.39940	10.54940
88630.416	HCN	$J = 1 \rightarrow 0, F = 1 \rightarrow 1$	-2.99110	8.91247	0.00000	4.25356
88631.848	HCN	$J = 1 \rightarrow 0, F = 2 \rightarrow 1$	-2.76930	14.85197	0.00000	4.25363
88633.936	HCN	$J = 1 \rightarrow 0, F = 0 \rightarrow 1$	-3.46820	2.97073	0.00000	4.25373
89188.525	HCO ⁺	$J = 1 \rightarrow 0$	-2.26080	15.21022	0.00000	4.28035
90663.568	HNC	$J = 1 \rightarrow 0$	-2.52180	9.30176	0.00000	4.35114
90979.023	HC ₃ N	$J = 10 \rightarrow 9$	-2.28480	139.25442	13.65650	24.01482
92494.308	¹³ CS	$J = 2 \rightarrow 1$	-2.80010	15.33521	1.54270	6.65859
93171.880	N ₂ H ⁺⁺	$J = 1 \rightarrow 0, F1 = 1 \rightarrow 1$	-2.78440	37.25038	0.00000	4.47152
93173.700	N ₂ H ⁺⁺	$J = 1 \rightarrow 0, F1 = 2 \rightarrow 1$	-2.56250	62.08887	0.00000	4.47161
93176.130	N ₂ H ⁺⁺	$J = 1 \rightarrow 0, F1 = 0 \rightarrow 1$	-3.26140	12.41913	0.00000	4.47172
218222.192	H ₂ CO	$3_{0,3} \rightarrow 2_{0,2}$	-2.76900	16.30796	7.28640	20.95640
219560.354	C ¹⁸ O	$J = 2 \rightarrow 1$	-4.17940	0.02440	3.66190	15.80580
220398.684	¹³ CO	$J = 2 \rightarrow 1$	-4.17490	0.04869	3.67590	15.86618
224714.385	C ¹⁷ O	$J = 2 \rightarrow 1$	-4.15090	0.02432	3.74790	16.17689

*. N₂H⁺ hyperfine multiplets are blended, we only list the three strongest hyperfine lines.

Table A2: Linewidth, the intensity integrated over the dispersion of each line (subtable I), and the integrated optical depth over the velocity dispersion of the strongest line among multiplet (subtable II).

Species	Freq ^I	G28.34 S		IRDC 18530		IRDC 18306		IRDC 18308	
I. Linewidth $\Delta\nu$ (km s ⁻¹) and integrated intensity $\int T_{\rm B}(\nu)d\nu$ (K km s ⁻¹) in four IRDCs									
	(GHz)	(km s ⁻¹)	(K km s ⁻¹)	(km s ⁻¹)	(K km s ⁻¹)	(km s ⁻¹)	(K km s ⁻¹)	(km s ⁻¹)	(K km s ⁻¹)
OCS	85.1391	3.91 ± 0.66	0.26 ± 0.04	×	×	—	≤ 0.05	—	≤ 0.06
c-C ₃ H ₂	85.3389	2.97 ± 0.10	1.51 ± 0.05	×	×	1.99 ± 0.12	0.69 ± 0.03	1.76 ± 0.23	0.34 ± 0.04
c-CH ₃ C ₂ H ⁽¹⁾	85.4557	3.08 ± 0.45	0.31 ± 0.04	×	×	2.21 ± 0.42	0.18 ± 0.03	2.81 ± 0.81	0.22 ± 0.06
c-CH ₃ C ₂ H ⁽²⁾	85.4573	2.44 ± 0.42	0.26 ± 0.04	×	×	1.08 ± 0.55	0.08 ± 0.03	—	≤ 0.08
NH ₂ D	85.9263	5.92 ± 1.04	0.41 ± 0.05			8.95 ± 1.16	0.32 ± 0.04	7.36 ± 1.53	0.21 ± 0.04
H ¹³ CO ⁺	86.7543	3.07 ± 0.06	1.32 ± 0.02	2.01 ± 0.06	0.55 ± 0.02	2.05 ± 0.10	0.50 ± 0.02	2.09 ± 0.09	0.59 ± 0.02
SiO	86.8470	4.83 ± 0.39	0.55 ± 0.03	—	≤ 0.03	—	≤ 0.25	—	≤ 0.03
HN ¹³ C	87.0909	2.99 ± 0.07	1.12 ± 0.02	1.71 ± 0.08	0.47 ± 0.02	2.24 ± 0.10	0.41 ± 0.02	2.08 ± 0.11	0.43 ± 0.02
HNCO	87.9244	2.68 ± 0.09	0.83 ± 0.02	1.75 ± 0.14	0.25 ± 0.02	2.13 ± 0.18	0.25 ± 0.02	2.11 ± 0.35	0.17 ± 0.02
HCO ⁺	89.1885	2.44 ± 0.08	5.27 ± 0.13	3.74 ± 0.05	4.74 ± 0.05	3.11 ± 0.28	1.72 ± 0.14	3.37 ± 0.06	5.52 ± 0.08
HNC	90.6636	2.59 ± 0.05	5.57 ± 0.08	3.10 ± 0.03	4.01 ± 0.03	2.94 ± 0.12	1.85 ± 0.07	2.83 ± 0.04	3.95 ± 0.05
HC ₃ N	90.979	3.36 ± 0.16	0.70 ± 0.03	2.22 ± 0.23	0.20 ± 0.02	2.34 ± 0.22	0.25 ± 0.02	3.03 ± 0.87	0.14 ± 0.03
¹³ CS	92.4943	3.06 ± 0.39	0.22 ± 0.02	—	≤ 0.03	2.28 ± 0.42	0.11 ± 0.02	—	≤ 0.03
H ₂ CO	218.222	3.73 ± 0.42	0.98 ± 0.09	—	≤ 0.15	—	≤ 0.15	—	≤ 0.14
C ¹⁸ O	219.56	3.70 ± 0.07	7.83 ± 0.13	2.42 ± 0.06	3.71 ± 0.08	1.95 ± 0.06	3.75 ± 0.10	1.94 ± 0.07	3.02 ± 0.10
¹³ CO	220.399	4.83 ± 0.20	21.18 ± 0.62	3.78 ± 0.13	16.24 ± 0.47	3.11 ± 0.25	9.79 ± 0.69	2.75 ± 0.13	14.15 ± 0.63
C ¹⁷ O	224.714	3.72 ± 0.25	2.35 ± 0.13	×	×	2.06 ± 0.12	1.26 ± 0.07	2.61 ± 0.36	0.70 ± 0.09
II. Linewidth $\Delta\nu$ (km s ⁻¹) and integrated optical depth $\tau_0\Delta\nu$ (km s ⁻¹) of the main line in four IRDCs									
	(GHz)	(km s ⁻¹)	(km s ⁻¹)	(km s ⁻¹)	(km s ⁻¹)	(km s ⁻¹)	(km s ⁻¹)	(km s ⁻¹)	(km s ⁻¹)
N ₂ H ⁺	93.1738	2.94 ± 0.01	1.14 ± 0.01	1.84 ± 0.04	1.20 ± 0.18	1.88 ± 0.03	1.19 ± 0.15	2.02 ± 0.02	0.20 ± 0.04
C ₂ H	87.3169	2.90 ± 0.07	4.00 ± 0.59	1.85 ± 0.08	0.91 ± 0.48	1.73 ± 0.07	3.10 ± 0.66	1.76 ± 0.11	0.18 ± 0.17
HCN	88.6318	2.33 ± 0.06	0.23 ± 0.10	3.23 ± 0.05	0.32 ± 0.04	2.60 ± 0.19*	25.80 ± 7.50*	3.15 ± 0.10	2.43 ± 0.83
H ¹³ CN	86.3402	2.96 ± 0.12	0.54 ± 0.19	2.25 ± 0.27*	0.23 ± 5.61*	1.82 ± 0.64*	0.62 ± 1.77*	1.69 ± 0.34*	0.17 ± 7.08*

Note. 1. Transition numbers are listed in Table A1;

2. Values are obtained from the Gaussian/hyperfine multiplets fit program based on CLASS;

3. Uncertainties on the measured intensities are typically ≤ 10%;

4. For species that are not detected, an upper limit equal to the 3 σ rms is given;5. “—” denotes < 3 σ detection in our dataset, and the intensity upper limit comes from the 3 σ rms of the entire region by integrating three channels in total around the V_{LSR} ;

6. “x” denotes no observations in our dataset;

7. “***” denotes a Hyperfine multiplet that is not well fitted.

Table A3: Velocity integration range for each line imaged in Figure 3.

Freq. (MHz)	Transition	G28.34 S (km s ⁻¹ –km s ⁻¹)	IRDC 18530 (km s ⁻¹ –km s ⁻¹)	IRDC 18306 (km s ⁻¹ –km s ⁻¹)	IRDC 18308 (km s ⁻¹ –km s ⁻¹)
85139.103	OCS	77.84–81.75	×	53.29–56.31 *	76.69–79.71 *
85338.894	c-C ₃ H ₂ (2 _{1,2} → 1 _{0,1})	76.92–79.89	×	53.51–55.49	76.91–78.49
85457.300	CH ₃ C ₂ H (5 ₀ → 4 ₀)	77.98–80.42	×	54.95–56.05	76.84–79.36
85926.278	NH ₂ D (1 _{1,1,0a} → 1 _{0,1,0a})	75.19–81.61	74.47–77.33	52.77–57.23	74.45–81.95
86340.163	H ¹³ CN (J = 1 → 0, F = 2 → 1)	76.92–79.88	73.31–76.69	52.94–54.66	76.16–77.84
86754.288	H ¹³ CO ⁺ (J = 1 → 0)	76.86–79.94	74.89–76.91	53.77–55.83	77.16–79.25
86846.960	SiO (J = 2 → 1)	75.98–80.81	74.39–77.41 *	53.29–56.31 *	75.49–78.51 *
87090.850	HN ¹³ C (J = 1 → 0)	76.91–79.89	74.84–76.56	53.88–56.12	77.16–79.24
87316.898	C ₂ H (N = 1 → 0, J = 3/2 → 1/2, F = 2 → 1)	76.95–79.85	74.97–76.83	53.53–55.27	76.12–77.88
87925.237	HNC (4 _{0,4} → 3 _{0,3})	77.06–79.74	74.12–75.88	53.73–55.87	75.41–78.59
88631.848	HCN (J = 1 → 0, F = 2 → 1)	77.23–79.56	73.4–78.4	53.5–56.1	76.62–79.78
89188.525	HCO ⁺ (J = 1 → 0)	77.18–79.62	73.4–78.4	53.24–56.35	76.52–79.89
90663.568	HNC (J = 1 → 0)	77.11–79.69	74.28–77.52	53.33–56.27	76.78–79.61
90979.023	HC ₃ N (J = 10 → 9)	76.72–80.08	74.79–77.01	53.63–55.97	76.74–78.86
92494.308	¹³ CS (J = 2 → 1)	78.47–81.53	74.39–77.41 *	54.43–55.57	77.49–80.51 *
93173.700	N ₂ H ⁺ (J = 1 → 0, F1 = 2 → 1)	76.93–79.87	74.98–76.82	53.86–55.74	77.19–79.21
21822.192	H ₂ CO	77.69–80.31	75.28–76.52 *	54.18–55.42 *	77.58–78.82 *
219560.354	C ¹⁸ O	76.55–80.25	74.69–77.11	53.83–55.77	77.23–79.17
220398.684	¹³ CO (J = 2 → 1)	75.98–80.81	74.01–77.79	53.24–56.35	76.83–79.58
224714.385	C ¹⁷ O (J = 2 → 1)	76.54–80.26	×	53.77–55.83	76.89–79.5

Note. 1. “×” denotes no observations in our dataset.2. “*” denotes a line having < 4σ detections; the integration range is given from three channels in total around the systematic V_{lsr} at its rest frequency.

Table A4: Average column densities and abundances for molecules with hyperfine multiplet lines in a square region from $[20'', 20'']$ to $[-20'', -20'']$ of four IRDCs observed by IRAM 30 m.

Species	G28.34 S		IRDC 18530		IRDC 18306		IRDC 18308	
	$T_{\text{ex},\alpha}$ (K)	(12 K)	$T_{\text{ex},\alpha}$ (K)	(9 K)	$T_{\text{ex},\alpha}$ (K)	(8 K)	$T_{\text{ex},\alpha}$ (K)	(12 K)
	I. Molecular Column density $[x \pm y(z) = (x \pm y) \times 10^z \text{ cm}^{-2}]$							
N_2H^+	$1.76 \pm 0.05(16)$	$1.46 \pm 0.02(15)$	$2.30 \pm 0.57(17)$	$2.94 \pm 0.43(15)$	$7.46 \pm 1.32(17)$	$4.24 \pm 0.51(15)$	$5.11 \pm 0.45(14)$	$2.59 \pm 0.49(14)$
C_2H	$4.93 \pm 0.80(14)$	$2.81 \pm 0.42(15)$	$1.59 \pm 0.73(14)$	$5.50 \pm 2.16(14)$	$3.63 \pm 0.84(14)$	$1.11 \pm 0.23(15)$	$3.09 \pm 4.83(13)$	$1.20 \pm 1.26(14)$
HCN	$4.40 \pm 2.83(13)$	$4.18 \pm 1.88(13)$	$7.15 \pm 0.47(13)$	$6.31 \pm 0.82(13)$	$1.68 \pm 0.31(17)$	$5.50 \pm 1.60(15)$	$3.06 \pm 0.11(15)$	$4.36 \pm 1.49(14)$
H^{13}CN	$9.27 \pm 0.28(14)$	$1.01 \pm 0.35(13)$	$5.70 \pm 62.60(14)$	$4.58 \pm 114.17(13)$	$6.94 \pm 6.64(15)^\dagger$	$8.11 \pm 23.23(14)$	$3.91 \pm 77.43(14)^\dagger$	$1.51 \pm 63.62(13)$
	II. Molecular Abundances with respect to H_2 $[x \pm y(z) = (x \pm y) \times 10^z]$							
N_2H^+	$1.33 \pm 1.49(-7)$	$1.11 \pm 0.18(-8)$	$1.34 \pm 1.15(-6)$	$1.72 \pm 0.53(-8)$	$3.91 \pm 4.29(-6)$	$2.22 \pm 1.11(-8)$	$8.35 \pm 9.49(-9)$	$4.24 \pm 2.04(-9)$
C_2H	$3.72 \pm 4.98(-9)$	$2.12 \pm 0.67(-8)$	$9.28 \pm 15.50(-10)$	$3.21 \pm 1.90(-9)$	$1.90 \pm 3.13(-9)$	$5.81 \pm 3.59(-9)$	$5.06 \pm 16.10(-10)$	$1.96 \pm 3.05(-9)$
HCN	$3.32 \pm 6.28(-10)$	$3.16 \pm 2.10(-10)$	$4.18 \pm 5.04(-10)$	$3.69 \pm 1.07(-10)$	$8.78 \pm 13.90(-7)$	$2.88 \pm 2.08(-8)$	$5.00 \pm 6.00(-8)$	$7.12 \pm 4.77(-9)$
H^{13}CN	$7.01 \pm 8.29(-9)$	$7.64 \pm 4.17(-10)$	$3.33 \pm 45.60(-9)$	$2.68 \pm 76.66(-10)$	$3.63 \pm 9.50(-8)^\dagger$	$4.24 \pm 17.63(-10)$	$6.40 \pm 166.00(-9)^\dagger$	$2.48 \pm 130.00(-10)$

Note. 1. Column densities and abundances in *italic font* are obtained at the temperatures listed in Table 6, under CTEX assumption;

2. Column densities and abundances in *roman font* are obtained at mean $T_{\text{ex,CO}}$ with LTE assumption;

3. Uncertainties on the measured values are determined from hyperfine multiplet fit to $\tau_0\Delta\nu$ and $T_{\text{ex},\alpha}$ or $T_{\text{ex,CO}}$;

4. “†” denotes a species whose distribution is less extended than the 30 m primary beam (filling factor $f < 0.5$).

Table A5: Average column densities and abundances for molecules without hyperfine multiplet lines in a square region from $[20'', 20'']$ to $[-20'', -20'']$ of four IRDCs observed by IRAM 30 m.

Species	G28.34 S (12 K)	IRDC 18530 (9 K)	IRDC 18306 (12 K)	IRDC 18308 (12 K)
I. Molecular Column density $[x \pm y(z) = (x \pm y) \times 10^z \text{ cm}^{-2}]$				
OCS	$2.31 \pm 0.34(13)$	x	$\leq 5.62(12)$	$\leq 5.32(12)$
c-C ₃ H ₂	$1.10 \pm 0.03(13)$	x	$3.61 \pm 0.17(12)$	$2.48 \pm 0.32(12)$
c-CH ₃ C ₂ H ⁽¹⁾	$5.01 \pm 0.69(13)$	x	$1.53 \pm 0.29(14)$ †	$3.52 \pm 0.92(13)$
c-CH ₃ C ₂ H ⁽²⁾	$2.23 \pm 0.33(13)$	x	$6.48 \pm 0.08(12)$	$\leq 7.09(12)$
NH ₂ D	$5.53 \pm 0.61(12)$	$6.60 \pm 0.80(12)$ †	$5.94 \pm 0.69(12)$	$2.79 \pm 0.52(12)$
H ¹³ CO ⁺	$1.45 \pm 0.03(12)$	$5.13 \pm 0.14(11)$	$4.39 \pm 0.19(11)$	$6.51 \pm 0.23(11)$
SiO	$1.11 \pm 0.07(12)$	$\leq 5.39(10)$	$\leq 4.34(11)$	$\leq 6.00(10)$
HN ¹³ C	$2.55 \pm 0.05(12)$	$9.13 \pm 0.35(11)$	$7.45 \pm 0.33(11)$	$9.69 \pm 0.45(11)$
HNCO	$1.75 \pm 0.05(13)$	$6.50 \pm 0.44(12)$	$7.22 \pm 0.56(12)$	$3.60 \pm 0.46(12)$
HCO ⁺ *	$4.42 \pm 0.11(13)$	$3.82 \pm 0.04(13)$	$2.32 \pm 0.18(13)$	$4.05 \pm 0.06(13)$
HNC*	$6.52 \pm 0.09(13)$	$4.02 \pm 0.03(13)$	$2.49 \pm 0.09(13)$	$3.97 \pm 0.05(13)$
HC ₃ N	$3.77 \pm 0.15(12)$	$1.58 \pm 0.14(12)$	$2.42 \pm 0.20(12)$	$7.42 \pm 1.43(11)$
¹³ CS	$9.95 \pm 1.08(11)$	$\leq 1.25(11)$	$4.66 \pm 0.82(11)$	$\leq 1.37(11)$
H ₂ CO	$7.36 \pm 0.64(13)$ †	$\leq 9.15(11)$	$\leq 9.67(11)$	$\leq 7.81(11)$
C ¹⁸ O	$4.48 \pm 0.07(15)$	$2.50 \pm 0.05(15)$	$2.78 \pm 0.07(15)$	$1.73 \pm 0.06(15)$
¹³ CO*	$3.41 \pm 0.10(16)$	$3.39 \pm 0.10(16)$	$2.01 \pm 0.09(16)$	$4.61 \pm 0.32(16)$
C ¹⁷ O	$1.33 \pm 0.07(15)$	x	$9.55 \pm 0.50(14)$	$3.97 \pm 0.54(14)$
II. Molecular Abundances with respect to H ₂ $[x \pm y(z) = (x \pm y) \times 10^z]$				
OCS	$1.75 \pm 0.55(-10)$	x	$\leq 2.94(-11)$	$\leq 8.70(-11)$
c-C ₃ H ₂	$8.31 \pm 1.53(-11)$	x	$1.89 \pm 0.75(-11)$	$4.05 \pm 1.64(-11)$
c-CH ₃ C ₂ H ⁽¹⁾	$3.79 \pm 1.17(-10)$	x	$8.03 \pm 4.70(-10)$ †	$5.75 \pm 3.27(-10)$
c-CH ₃ C ₂ H ⁽²⁾	$1.69 \pm 0.54(-10)$	x	$3.39 \pm 2.59(-11)$	$\leq 1.16(-10)$
NH ₂ D	$4.18 \pm 1.16(-11)$	$3.85 \pm 1.09(-11)$ †	$3.11 \pm 1.52(-11)$	$4.56 \pm 2.18(-11)$
H ¹³ CO ⁺	$1.09 \pm 0.19(-11)$	$3.00 \pm 0.52(-12)$	$2.30 \pm 0.90(-12)$	$1.06 \pm 0.31(-11)$
SiO	$8.35 \pm 1.82(-12)$	$\leq 3.15(-13)$	$\leq 2.27(-12)$	$\leq 9.81(-13)$
HN ¹³ C	$1.93 \pm 0.33(-11)$	$5.33 \pm 1.00(-12)$	$3.90 \pm 1.54(-12)$	$1.58 \pm 0.48(-11)$
HNCO	$1.32 \pm 0.24(-10)$	$3.79 \pm 0.84(-11)$	$3.79 \pm 1.66(-11)$	$5.89 \pm 2.38(-11)$
HCO ⁺ *	$3.34 \pm 0.59(-10)$	$2.23 \pm 0.35(-10)$	$1.21 \pm 0.54(-10)$	$6.63 \pm 1.74(-10)$
HNC*	$4.58 \pm 0.76(-10)$	$2.18 \pm 0.33(-10)$	$1.56 \pm 0.60(-10)$	$6.49 \pm 1.69(-10)$
HC ₃ N	$2.85 \pm 0.56(-11)$	$9.25 \pm 2.26(-12)$	$1.26 \pm 0.56(-11)$	$1.21 \pm 0.59(-11)$
¹³ CS	$7.52 \pm 2.06(-12)$	$\leq 7.30(-13)$	$2.44 \pm 1.39(-12)$	$\leq 2.25(-12)$
H ₂ CO	$5.56 \pm 1.39(-10)$ †	$\leq 5.35(-12)$	$\leq 5.06(-12)$	$\leq 1.28(-11)$
C ¹⁸ O	$3.38 \pm 0.57(-8)$	$1.46 \pm 0.24(-8)$	$1.46 \pm 0.54(-8)$	$2.83 \pm 0.80(-8)$
¹³ CO*	$2.58 \pm 0.47(-7)$	$1.98 \pm 0.35(-7)$	$2.41 \pm 1.04(-7)$	$3.28 \pm 0.98(-7)$
C ¹⁷ O	$1.01 \pm 0.21(-8)$	x	$5.00 \pm 2.02(-9)$	$6.50 \pm 2.69(-9)$

Note. I. “x” denotes a species that we did not observe in a certain source;

2. For species that are not detected, an upper limit derived from 3σ rms is given;

3. Column density and abundances are obtained at mean T_{ex} of CO isotopologues with LTE assumption;

4. Species with “*” and values in bold face are likely obtained from optically thick lines and for which we did the optical depth correction;

5. Uncertainties on the measured values are determined from T_{ex} , CO, partition function $Q(T_{\text{ex}}, \text{CO})$, and Gaussian fit to $\int T_{\text{B}}(\nu) d\nu$;

6. “†” denotes a species whose distribution is less extended than the 30 m primary beam (filling factor $f < 0.5$).

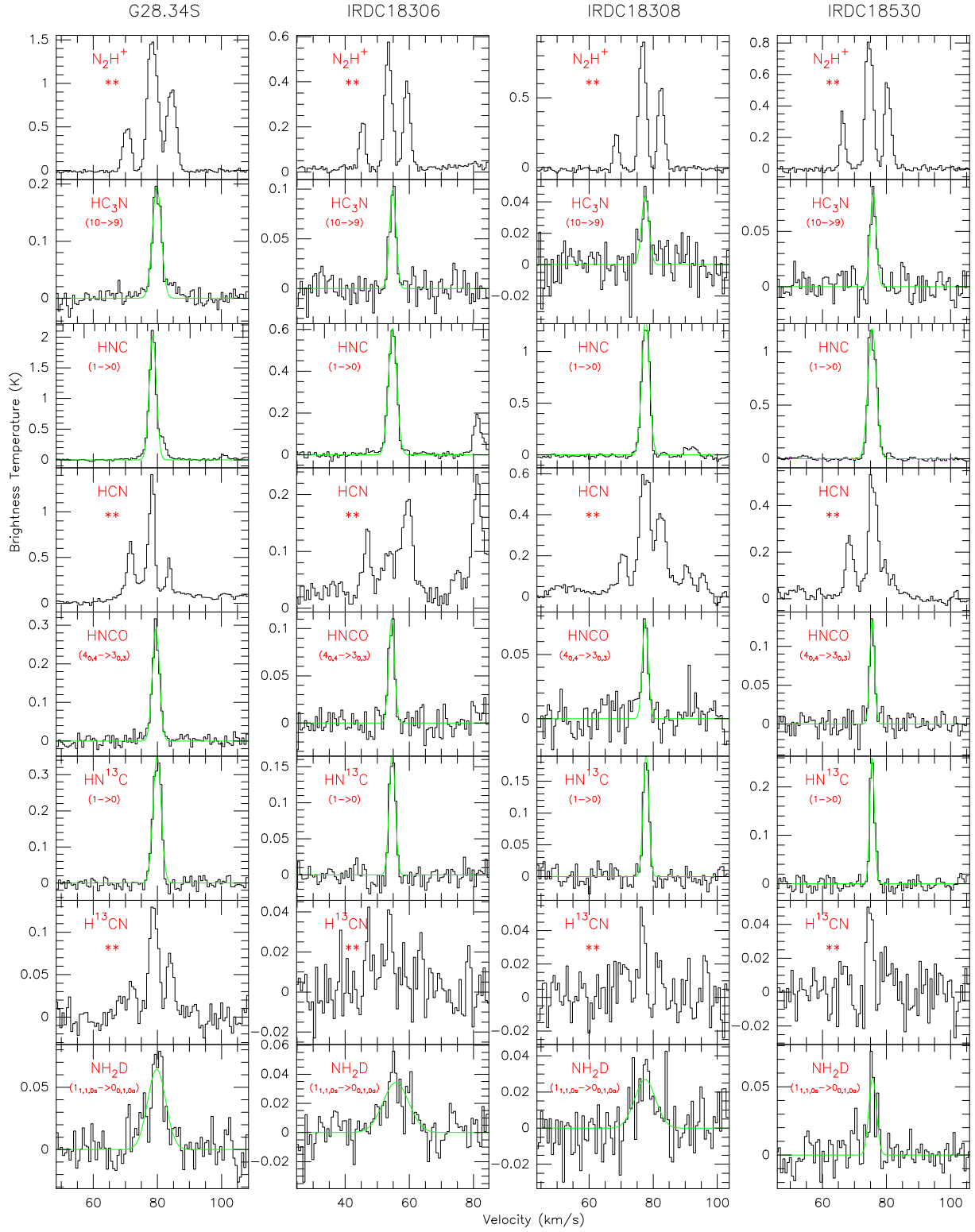


Fig. A1: Line profiles of identified species toward each IRDC, ordered in groups as described in Section 3.2.2. The green line is from a single-Gaussian fit. “**” denotes a species with hyperfine multiplets whose HFS fits are plotted in Figure 5. Profiles in blue denote the lines we detect from the “extra band” where the rms are higher than the others owing to less observation time.

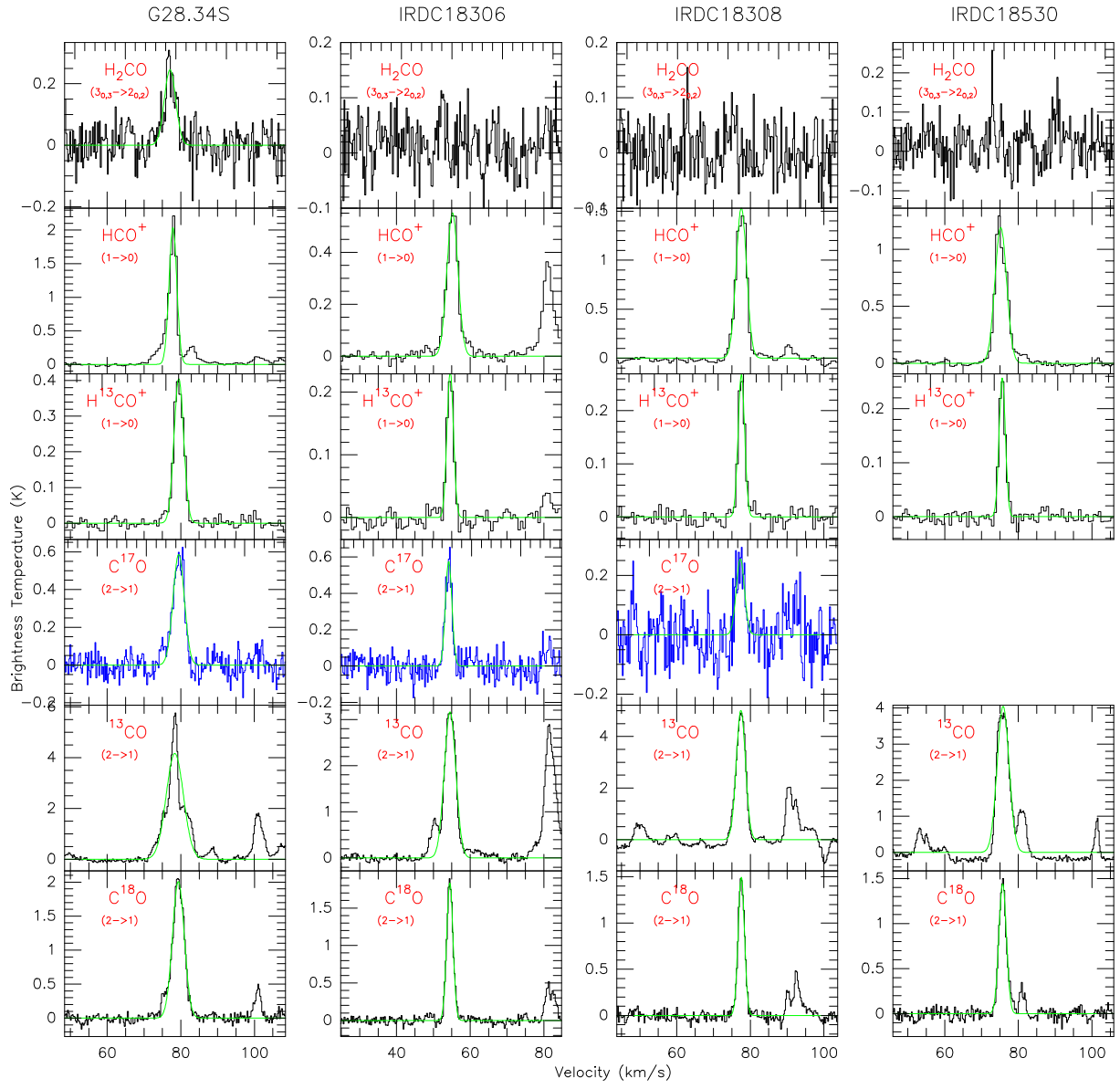
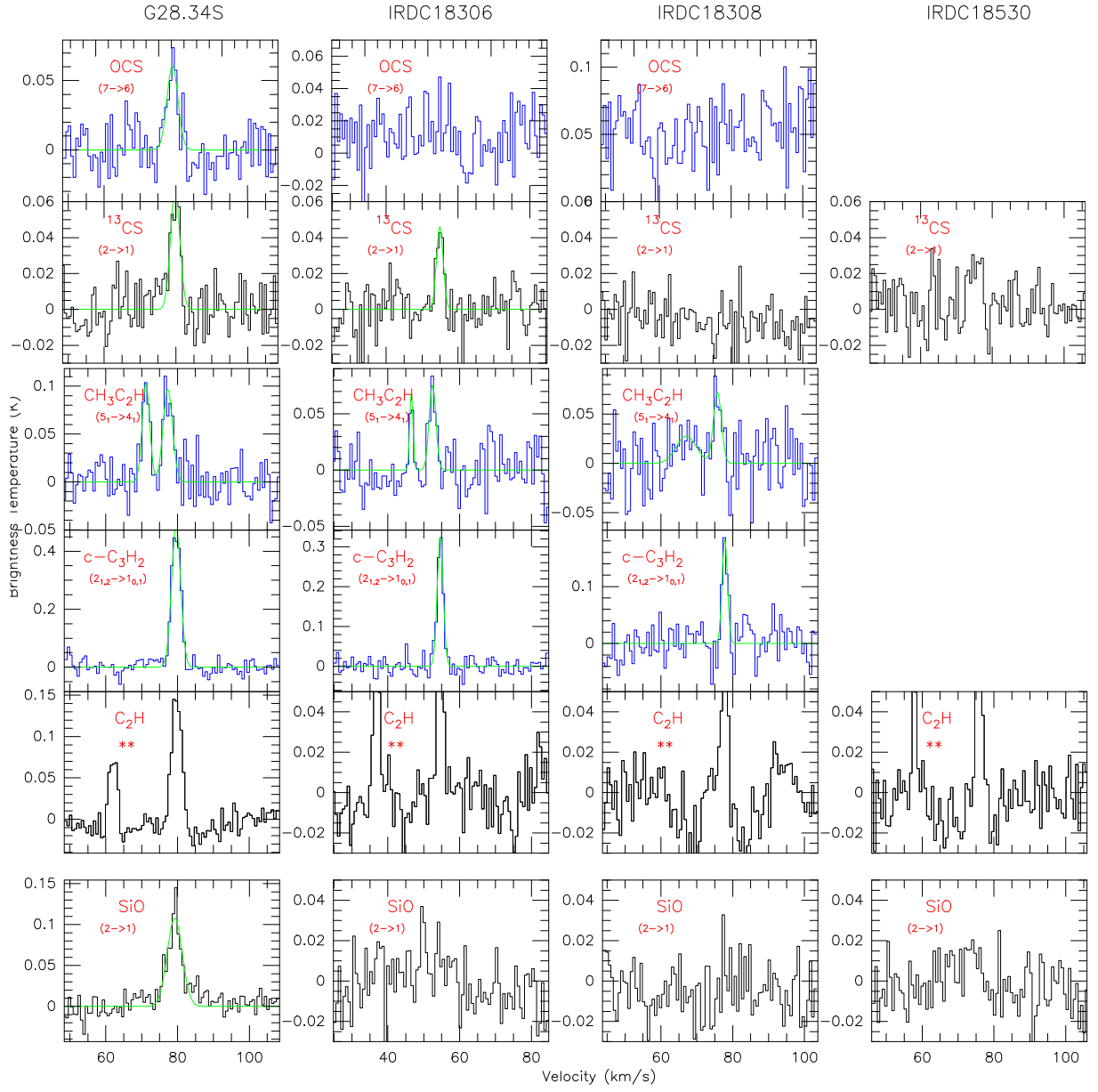


Fig. A1: (continued)



Note: Here a part of the multiplets of C_2H are shown; the complete set of multiplets is in Figure 5

Fig. A1: (continued)